

## MEASUREMENT OF THE SOLAR ELECTRON NEUTRINO FLUX WITH THE HOMESTAKE CHLORINE DETECTOR

BRUCE T. CLEVELAND, TIMOTHY DAILY, RAYMOND DAVIS, JR., JAMES R. DISTEL, KENNETH LANDE,<sup>1</sup>  
C. K. LEE, AND PAUL S. WILDENHAIN

Department of Physics and Astronomy, University of Pennsylvania, 209 South 33rd Street, Philadelphia, PA 19104

AND

JACK ULLMAN

Department of Physics and Astronomy, Herbert Lehman College (City University of New York), 250 Bedford Park Boulevard West, Bronx, NY 10468

Received 1996 April 22; accepted 1997 October 17

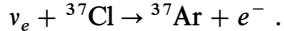
### ABSTRACT

The Homestake Solar Neutrino Detector, based on the inverse beta-decay reaction  $\nu_e + {}^{37}\text{Cl} \rightarrow {}^{37}\text{Ar} + e^-$ , has been measuring the flux of solar neutrinos since 1970. The experiment has operated in a stable manner throughout this time period. All aspects of this detector are reviewed, with particular emphasis on the determination of the extraction and counting efficiencies, the key experimental parameters that are necessary to convert the measured  ${}^{37}\text{Ar}$  count rate to the solar neutrino production rate. A thorough consideration is also given to the systematics of the detector, including the measurement of the extraction and counting efficiencies and the nonsolar production of  ${}^{37}\text{Ar}$ . The combined result of 108 extractions is a solar neutrino-induced  ${}^{37}\text{Ar}$  production rate of  $2.56 \pm 0.16$  (statistical)  $\pm 0.16$  (systematic) SNU.

*Subject headings:* elementary particles — Sun: interior — Sun: particle emission

### 1. INTRODUCTION

The Homestake solar neutrino experiment was built in the period 1965–1967 to measure the total flux of solar neutrinos above 0.814 MeV. A radiochemical technique is used, based on the inverse beta reaction



This method was first suggested by Pontecorvo (1946) and later independently proposed by Alvarez (1949). The construction of the Homestake experiment was stimulated by the measurement of the cross section for the  ${}^3\text{He}({}^4\text{He}, \gamma){}^7\text{Be}$  reaction by Holmgren & Johnston (1959). The measured cross section was higher than that anticipated by theoretical arguments and indicated that this reaction could compete, perhaps favorably, with the then-accepted termination of the solar energy-generating Bethe-Critchfield proton-proton fusion chain,  ${}^3\text{He}({}^3\text{He}, 2p){}^4\text{He}$ . It followed that two additional branches in the termination chain were significant, the now-familiar PPII and PPIII branches (Fowler 1958; Cameron 1958). These branches involved two additional, higher energy neutrino sources, those from electron capture on  ${}^7\text{Be}$  and those from the beta decay of  ${}^8\text{B}$  following the reaction  ${}^7\text{Be}(p, \gamma){}^8\text{B}$ ; both of these sources yield neutrinos above the 0.814 MeV energy threshold of the  ${}^{37}\text{Cl}-{}^{37}\text{Ar}$  absorption reaction. (A list of neutrino-producing reactions occurring in the Sun is given in Table 1, together with the energies of the resulting neutrinos and their capture cross sections on  ${}^{37}\text{Cl}$ . Cross sections for all reactions except the  ${}^8\text{B}$  reaction are taken from Bahcall 1989; the  ${}^8\text{B}$  cross section is from Bahcall et al. 1996.) Furthermore, it was found that the neutrino capture cross section for  ${}^{37}\text{Cl}$  is greatly enhanced above 5.8 MeV, due to the transition of the ground state of the  ${}^{37}\text{Cl}$  nucleus to its isobaric analog state in  ${}^{37}\text{Ar}$ , making the chlorine experiment particularly sensitive to the energetic neutrinos from

${}^8\text{B}$  decay (Bahcall 1964). Solar model calculations including these revised termination chains indicated that a large-scale  ${}^{37}\text{Cl}-{}^{37}\text{Ar}$  radiochemical detector could observe a measurable flux of neutrinos.

The initial observations with the Homestake detector showed that the solar neutrino flux was less than 3 SNU (Davis, Harmer, & Hoffman 1968), well below the solar model prediction (Bahcall, Bahcall, & Shaviv 1968). (One solar neutrino unit = one interaction per  $10^{36}$  target atoms s $^{-1}$ .) A series of tests were performed to verify that the detector was operating properly and was capable of observing the anticipated solar neutrino signal. These tests demonstrated that both isotopically labeled argon gas that was introduced into and thoroughly mixed with the detector liquid and  ${}^{37}\text{Ar}$  that was produced by a neutron source in the center of the tank could be quantitatively recovered (Davis et al. 1968). The number of  ${}^{37}\text{Ar}$  atoms from both the neutron tests and the solar neutrino observations was measured by looking for their decay in a miniature proportional counter using only pulse height analysis to select events in the Auger electron peak. Although a clean signal was observed for the neutron activation tests, no events above background were observed in the solar neutrino samples, resulting in the upper limit given above.

Fortunately it was found that adding a pulse rise time restriction to the event selection procedure could improve signal versus background discrimination sufficiently that  ${}^{37}\text{Ar}$  decay events could be distinguished from background pulses in the solar neutrino samples. Rise time counting was introduced in late 1970 starting with run 18. Early results employing this detection technique were presented at the Irvine conference (Trimble & Reines 1972).

A history of the development of the Homestake experiment is given in Bahcall & Davis (1982). Periodically, reports of the average neutrino-induced production rate observed, together with descriptions of the operation of the detector and the many tests that have been performed to verify its proper operation, have appeared in various conference proceedings; see, for example, Bahcall & Davis

<sup>1</sup> Electronic inquiries may be addressed to klande@mail.sas.upenn.edu.

TABLE 1  
NEUTRINO-PRODUCING REACTIONS IN THE SUN

Reaction	$E_\nu$ (MeV)	$\sigma$ ( $\text{cm}^2$ )
<b>Proton-Proton Chain:</b>		
Phase I:		
$p + p \rightarrow d + e^+ + \nu_e$ .....	$\leq 0.420$	0
$p + e^- + p \rightarrow d + \nu_e$ .....	1.442	$16 \times 10^{-46}$
$p + d \rightarrow {}^3\text{He} + \gamma$ .....		
${}^3\text{He} + {}^3\text{He} \rightarrow {}^4\text{He} + p + p$ .....		
${}^3\text{He} + p \rightarrow {}^4\text{He} + e^+ + \nu_e$ .....	$\leq 18.8$	$3.9 \times 10^{-42}$
Phase II:		
${}^3\text{He} + {}^4\text{He} \rightarrow {}^7\text{Be} + \gamma$ .....		
${}^7\text{Be} + e^- \rightarrow {}^7\text{Li} + \nu_e$ .....	0.861 (90%)	$2.4 \times 10^{-46}$
${}^7\text{Li} + p \rightarrow {}^4\text{He} + {}^4\text{He}$ .....		
Phase III:		
${}^7\text{Be} + p \rightarrow {}^8\text{B} + \gamma$ .....		
${}^8\text{B} \rightarrow {}^8\text{Be}^* + e^+ + \nu_e$ .....	$\leq 15$	$1.14 \times 10^{-42}$
${}^8\text{Be}^* \rightarrow {}^4\text{He} + {}^4\text{He} + \gamma$ .....		
<b>Carbon-Nitrogen Cycle:</b>		
$p + {}^{12}\text{C} \rightarrow {}^{13}\text{N} + \gamma$ .....		
${}^{13}\text{N} \rightarrow {}^{13}\text{C} + e^+ + \nu_e$ .....	$\leq 1.20$	$1.7 \times 10^{-46}$
$p + {}^{13}\text{C} \rightarrow {}^{14}\text{N} + \gamma$ .....		
$p + {}^{14}\text{N} \rightarrow {}^{15}\text{O} + \gamma$ .....		
${}^{15}\text{O} \rightarrow {}^{15}\text{N} + e^+ + \nu_e$ .....	$\leq 1.73$	$6.8 \times 10^{-46}$
$p + {}^{15}\text{N} \rightarrow {}^{12}\text{C} + {}^4\text{He}$ .....		

NOTE.—Capture cross sections for  $\nu_e$  on  ${}^{37}\text{Cl}$  for all sources except the  ${}^8\text{B}$  reaction are taken from Bahcall 1989; the  ${}^8\text{B}$  cross section is from Bahcall et al. 1996.

(1976), Davis (1978, 1993, 1994a, 1994b), Cleveland, Davis, & Rowley (1980), Cleveland et al. (1990, 1995), Davis, Cleveland, & Rowley (1982), Lande et al. (1991), and Rowley, Cleveland, & Davis (1984).

Due to the extremely small production rate of  ${}^{37}\text{Ar}$  in the detector, the uncertainty of a single solar neutrino observation is dominated by the statistical uncertainty in the number of  ${}^{37}\text{Ar}$  atoms observed. The accumulation of counts over the 25 years of observation now results in a statistical error on the average production rate of about 6%, comparable to that due to systematic effects. A careful review of the systematics of the detector, including consideration of the extraction efficiency, counting efficiency, and nonsolar production of  ${}^{37}\text{Ar}$ , has recently been completed, quantifying the contribution of systematic effects to the uncertainty of the average production rate to be 6.1%.

The purpose of the present report is to review the operation of the detector, the tests validating that operation, and the systematic uncertainties applicable to the measurement and to provide an up-to-date account of the results of both the individual solar neutrino observations and the cumulative average.

Section 2 of this report describes the determination of the neutrino capture cross section on  ${}^{37}\text{Cl}$ ; although this parameter is crucial to the interpretation of our results, the measurements and calculations have been carried out by other investigators, so we have been deliberately brief. The reader is encouraged to consult the references for details concerning these difficult and important experiments. Section 3 gives an account of the location, construction, and physical layout of the detector apparatus, together with a brief overview of the operational procedure. Section 4 gives a detailed description of the procedure for the recovery and purification of argon from the tank, together with results of various tests made to validate this procedure. Section 5 details the procedure for counting the number of  ${}^{37}\text{Ar}$  atoms extracted; § 6 describes the nonsolar processes that produce  ${}^{37}\text{Ar}$  in the detector. Finally, § 7 gives an account of

the analysis of the data, including discussion of the statistical and systematic uncertainties, together with the results of the 108 individual observations made between 1970 and 1994 and the average production rate over that time period. There are also two appendices that discuss specific topics in greater detail: Appendix A describes the measurements and calculations involved in determining the extraction efficiency, and Appendix B discusses the procedure for calibrating counter efficiencies.

## 2. NEUTRINO CAPTURE CROSS SECTION OF ${}^{37}\text{Cl}$

The cross section for reactions that go directly from  ${}^{37}\text{Cl}$  to the ground state of  ${}^{37}\text{Ar}$  can be calculated as a function of the neutrino energy from the principle of detailed balancing, the known parameters of the ground states of  ${}^{37}\text{Ar}$  and  ${}^{37}\text{Cl}$ , and the lifetime of  ${}^{37}\text{Ar}$  (Bahcall 1978). This allows the determination of the interaction cross section for the intermediate-energy solar neutrinos ( ${}^7\text{Be}$ ,  ${}^8\text{B}$ , and CNO), as the neutrinos from each of these sources are only energetic enough to excite the transition to the  ${}^{37}\text{Ar}$  ground state.

The cross sections for the more energetic  ${}^8\text{B}$  decay neutrinos, which can feed numerous excited states in  ${}^{37}\text{Ar}$ , can be calculated from the beta decay of  ${}^{37}\text{Ca}$  (Bahcall & Barnes 1964). The decay of  ${}^{37}\text{Ca}$  to various excited states in  ${}^{37}\text{K}$  is the isospin mirror of the neutrino absorption in  ${}^{37}\text{Cl}$  to the equivalent states in  ${}^{37}\text{Ar}$ . Measurements of the branching ratios for  ${}^{37}\text{Ca}$  decays to excited states in  ${}^{37}\text{K}$  permit determination of the  $ft$ -values for the individual transitions and thereby the cross sections for  ${}^{37}\text{Cl}$  to these states in  ${}^{37}\text{Ar}$ . A number of these states have low  $ft$ -values, especially the superallowed analog state at 5.0 MeV, making the chlorine detector especially sensitive to neutrinos with  $E > 5.8$  MeV.

The cross section for neutrino capture by nuclei can also be evaluated by studying  $(p, n)$  reactions in the forward direction at high proton energies (60 MeV and higher) (Goodman et al. 1980). Evaluation of the cross section for  $\nu_e$  from  ${}^8\text{B}$  decay on  ${}^{37}\text{Cl}$ , using all available nuclear physics inputs, including recent beta decay and  $(p, n)$  studies (Garcia et al. 1991; Wells 1992), gives  $(1.11 \pm 0.044) \times 10^{-42} \text{ cm}^2$  (Aufderheide et al. 1994). A reexamination of the expected  ${}^8\text{B}$  neutrino energy spectrum from the Sun has slightly changed this cross section to  $(1.14 \pm 0.037) \times 10^{-42} \text{ cm}^2$  (Bahcall et al. 1996).

## 3. THE HOMESTAKE SOLAR NEUTRINO OBSERVATORY

### 3.1. Description of Facilities

The Homestake Solar Neutrino Observatory is located in the Homestake Gold Mine, at Lead, South Dakota (lat.  $44^\circ 20' \text{ N}$ , long.  $103^\circ 50' \text{ W}$ ). The Homestake mine, which has been in continuous operation since 1876, is the deepest operating mine in the continental US, with workings down to a depth of 2500 m below the surface level. We were indeed fortunate in being able to use this very deep mine to build our neutrino detector. Homestake's mining and engineering expertise was essential in building the observatory and in operating it for the last 30 years.

The observatory chamber is located on the 4850 ft level of the mine (1478 m from the surface), 200 m from the base of the Yates shaft, the main access to the mine. Integration over surface contours and rock densities gives an average overburden for the detector of  $4200 \pm 100$  meters water

equivalent (m.w.e.). Excavation of the chamber was carried out by the Homestake Mining Company during the period 1965 January to 1965 September. Fortunately, the rock wall is both structurally sound and relatively low in uranium and thorium. The bare wall is covered with chain-link fencing bolted to the wall with rock bolts 1.5 m long to ensure stability. The floor is covered with 5 cm of concrete.

Figure 1 shows the arrangement of the detector elements in the rock cavity. The apparatus consists of a single horizontal steel tank with dished ends, 6.1 m in diameter and 14.6 m long, containing 615 metric tons of tetrachloroethylene,  $C_2Cl_4$ . The tetrachloroethylene fills about 95% of the detector volume with the remaining 5% filled with helium gas at 1.5 atm pressure (absolute). The tank is set below the entrance adit so that the cavity can be flooded with water to shield the detector from fast neutrons from the rock wall. A 5 cm diameter reentrant tube is provided in the middle of the tank, which permits placement of a neutron source for extraction efficiency tests at the tank center [ $^{37}Ar$  is produced by  $(n, p)$  followed by  $(p, n)$  reactions]. There are also provisions to allow the insertion of a neutrino source for a direct calibration of the detector. Two liquid circulation pumps are located in an adjacent

room that is separated from the detector chamber by a watertight door and is accessed by an inclined tunnel.

The tank was built by the Chicago Bridge and Iron Company, an excellent engineering company that had considerable experience in building large vacuum chambers for space equipment testing. The company was extremely helpful in complying with our unusual requirements. The design and construction of the detector were driven by two paramount concerns. First, because the Earth's atmosphere contains 0.934% argon, it was essential that the tank and all associated piping be absolutely leakproof. This is a rigid requirement because the sensitivity of the detector depends upon extracting a small volume of argon carrier gas and placing the final sample into a proportional counter with an internal volume of only  $0.5 \text{ cm}^3$ . The system was helium vacuum-leak tested by providing a blanket of helium around the tank and searching for the presence of helium inside the tank. The upper limit on the inleakage of helium, less than  $10^{-6} \text{ cm}^3 \text{ s}^{-1}$ , was limited by the sensitivity of the method.

The second major concern in constructing the tank was to minimize the radioactivity of the materials, in order to ensure that the nonsolar production of  $^{37}Ar$  from these

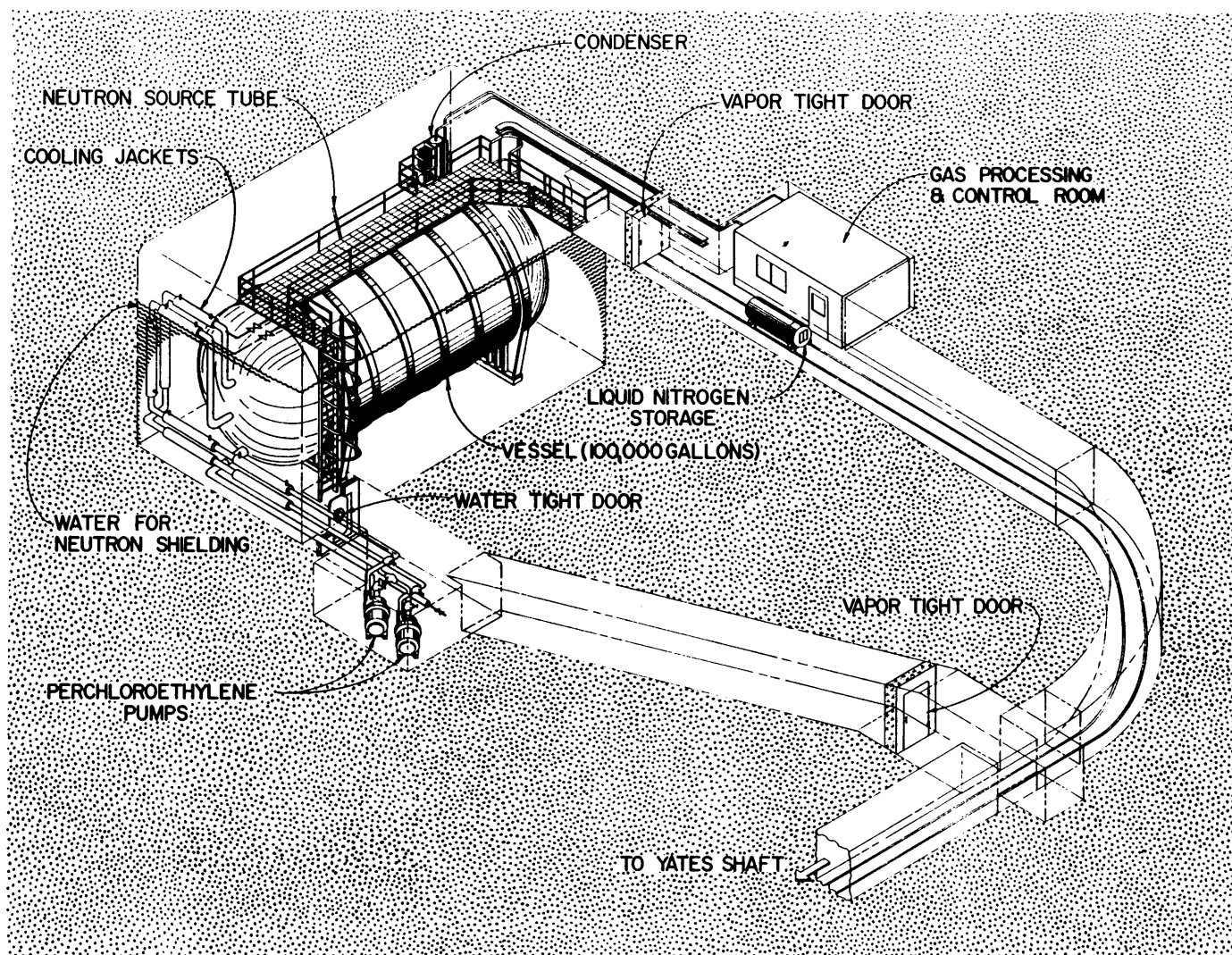


FIG. 1.—Homestake solar neutrino experiment. Arrangement of the detector elements in the rock cavity, 1478 m below the surface in the Homestake Gold Mine.

sources was less than that from solar neutrinos. Prior to fabrication of the tank parts, the steel to be used was tested for surface  $\alpha$ -particle activity to ensure that it would meet our requirements. These parts were then welded in place underground, using welding rod and flux that did not contain thorium. The  $\alpha$ -particle activity of the inside surface of the tank, all the piping, and the tetrachloroethylene were measured prior to filling the tank. The mine air, as in all underground locations, contains radon; we thus took the precaution of purging the inside of the tank with radon-free air before filling the system with  $C_2Cl_4$ . These procedures are described in more detail in § 6.3.

### 3.2. Neutrino Flux Determination Procedure

Solar neutrinos convert a very small number of the  $^{37}Cl$  atoms in the  $C_2Cl_4$  into  $^{37}Ar$ . The experimental problem is to remove these  $^{37}Ar$  atoms efficiently from the detector and determine their number. The fundamental equation describing the operation of the detector is

$$[N(^{37}Cl)] \sum \phi_i \sigma_i = \frac{N_c \lambda}{\epsilon_e \epsilon_c (1 - e^{-\lambda t_{exp}})} - p_{ns}.$$

The left-hand side of this equation gives the expected production rate of  $^{37}Ar$  in the detector due to the flux of solar neutrinos; the summation is over the various neutrino-producing reactions in the solar core, where  $\phi_i$  is the flux of electron neutrinos due to each source incident on the detector and  $\sigma_i$  is the flux-weighted cross section for the  $^{37}Cl(v_e, e^-)^{37}Ar$  reaction for such neutrinos (see Table 1).  $N(^{37}Cl)$  is the number of target  $^{37}Cl$  nuclei in the detector.

The first term on the right-hand side of this equation gives the total production rate of  $^{37}Ar$  measured in the detector. The total number of  $^{37}Ar$  atoms present in the detector at the time of extraction is given by the number of observed  $^{37}Ar$  decays,  $N_c$  (100% counting "ON time" has been assumed for simplicity), divided by the efficiency for extracting argon from the detector,  $\epsilon_e$ , and the efficiency of counting  $^{37}Ar$  decays,  $\epsilon_c$ . Because the  $^{37}Ar$  atoms begin to decay back to  $^{37}Cl$  within the tank even as they are created, the total number of  $^{37}Ar$  atoms in the tank grows only to a saturation level where the production rate is equal to the decay rate; the growth curve is described by the saturation fraction  $1 - e^{-\lambda t_{exp}}$  ( $t_{exp}$  is the exposure time of the tank for a given observation). Dividing the total number of  $^{37}Ar$  atoms by the saturation fraction and multiplying by the  $^{37}Ar$  decay constant,  $\lambda = 0.0198 \text{ day}^{-1}$ , gives the overall production rate,  $p$ , of  $^{37}Ar$  in the tank.

The known rate of nonsolar  $^{37}Ar$  production in the detector,  $p_{ns}$ , is subtracted from the overall production rate  $p$  to determine the observed production rate due to solar neutrinos; this expression is then set equal to the expected production rate. Of course, since the signal in the chlorine detector is due to a number of source reactions in the Sun, this measurement alone does not uniquely determine the flux from any one source but can be considered as an upper limit on the flux of electron neutrinos from each source. When its results are used in conjunction with those of other detectors of differing energy sensitivity, the flux of neutrinos from each source can be experimentally determined.

## 4. EXTRACTION AND PROCESSING OF ARGON

Since argon is a light noble gas, it will not chemically or physically (van der Waals) attach to tetrachloroethylene.

Dissolved argon is easily removed from the  $C_2Cl_4$  by purging the liquid with helium. The argon then can be removed from the helium gas stream with a suitable absorber. Finally, the argon sample is chemically purified and inserted into a small proportional counter to determine the number of  $^{37}Ar$  atoms recovered.

### 4.1. Removing Argon from Tetrachloroethylene

The system for removing the argon from the tank is illustrated in Figure 2. This procedure involves two steps: first, establishing and maintaining equilibrium between the argon in the gas phase and the argon dissolved in the liquid by bubbling the helium atmosphere through the tetrachloroethylene, and second, in parallel with the liquid-gas mixing cycle, sweeping the helium atmosphere of the tank through an external, cryogenically cooled absorber that traps the argon but allows the helium to pass through and return to the detector. As the argon in the gas reservoir is depleted due to adsorption onto the absorber, the liquid-gas mixing process restores equilibrium by transferring additional argon from the detector liquid to the gas.

Both of these gas cycles are driven by the detector's liquid pumping system. The tank is equipped with two liquid circulation pumps (approximate flow rate 1500 liters per minute). Each pump draws liquid uniformly from a common suction line at the bottom of the tank and returns it to the tank through a separate header pipe into a set of 20 eductor nozzles. The two header pipes are 2 and 4 m above the tank bottom, respectively. These eductors are Bernoulli effect devices in which a constriction of the fluid flow causes a pressure drop, resulting in suction that draws helium into the liquid and discharges the gas mixed with the liquid as a jet of very fine bubbles. Thirty-eight of the 40 eductors draw helium from the top of the tank while the remaining two eductors drive the helium through the external extraction system. During an extraction, the pump-eductor system continuously circulates the helium atmosphere that occupies the top 5% of the volume of the tank through the liquid at a rate of approximately 17,000 liters per minute (resulting in almost one complete circulation of the atmosphere each minute). This extremely fast recirculation rapidly establishes argon solubility equilibrium between the gas and liquid phases. Since argon is highly soluble in tetrachloroethylene (Clever et al. 1957; Saylor & Battino 1958), the resulting equilibrium distribution has about 1/10 of the argon in the gas phase and 9/10 of the argon dissolved in the liquid.

The first two eductors at the end of the upper header pipe are used to draw the helium through the argon recovery system. The argon-containing helium leaves the tank at the opposite end through a condenser at  $-40^\circ C$ . This serves to freeze out most of the tetrachloroethylene vapors, which return to the tank when the condenser is warmed at the end of extraction. After leaving the condenser, the gas flows from the detector room to the processing room, where it first flows through a laminar differential pressure gas flow meter, which measures the volume of He gas circulating through the recovery system, and then through a molecular sieve trap (10 kg of 13X pellets) that removes residual tetrachloroethylene vapors. The dry gas now passes through a countercurrent heat exchanger to a liquid nitrogen-cooled charcoal trap, on which the argon is adsorbed. The helium then flows back out through the heat exchanger and returns to the tank by means of the two eductors described above.

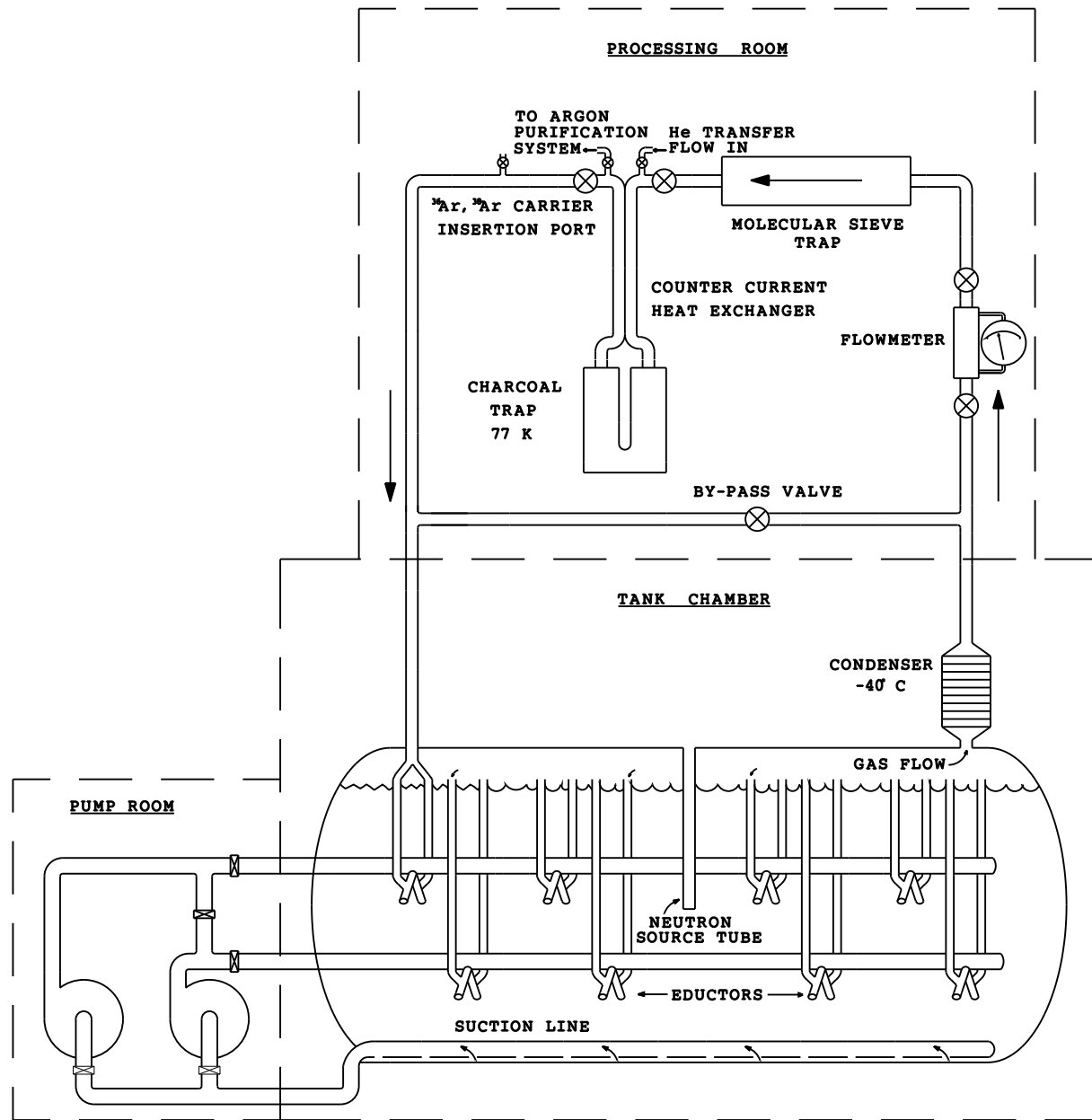


FIG. 2.—Schematic of Homestake solar neutrino experiment. Functional arrangement of the detector elements described in § 3. For purposes of clarity, the drawing shows only four pairs of eductors attached to each header pipe within the  $C_2Cl_4$  tank; there are actually 10 pairs on each pipe.

The rate of gas flow through the argon recovery system is 350 liters per minute. This flow remains constant at constant pumping speed because it is determined by the flow dynamics of the two eductors and the fixed impedance of the gas lines, condenser, and absorbers. The pressure drop developed across the recovery apparatus (1.8 psi) is continuously monitored during an extraction by gauges at the inflow and outflow of the processing room. Approximately 20 hr of gas flow are required to attain an argon recovery of 95%.

As indicated in Figure 2, bellows valves are placed in the suction and discharge lines of each liquid circulation pump. There is also a bypass line controlled by a valve between the two pumps. This arrangement allows removal of a pump, if necessary, without interrupting the operation of the extraction system, and makes it possible to operate the experi-

ment with one pump. Initially, two Chempumps of a standard canned-rotor design were used to drive the liquid circulation. Eventually, both of these pumps failed, resulting in a gap in the observational record between 1985 May and 1986 October. The Chempumps were replaced by a canned-rotor Pacific pump (in 1986) and a magnetically coupled Kontro pump (in 1988). The experiment has thus been operated at different times by either one or two pumps, from a variety of manufacturers.

These pump changes have had no effect on the relationship between total helium flow through the extraction system and extraction efficiency of the detector, as monitored individually for each run by the insertion and recovery of isotopically pure argon carrier (see § 4.3). These measurements show no dependence of the extraction rate on any particular pump configuration, indicating that the

argon is removed from the gas phase by the charcoal trap at a much slower rate than that at which the liquid-vapor solubility equilibrium is established by the recirculation of the helium atmosphere. Owing to the superior reliability of the magnetically coupled pump, we have continued operations using just the Kontro pump.

#### 4.2. Purification of Argon

The next procedure is to remove the sample from the charcoal trap, purify it by removing all non-argon gases from the sample, determine the volume of the remaining gas, and finally insert it into a proportional counter. Purification consists of two steps. First, active gases such as oxygen and nitrogen are removed by exposing the sample to titanium metal powder heated to 900°C in a quartz furnace and converting them to titanium oxide and titanium nitride. Second, other rare gases are separated from the argon by gas chromatography.

The extraction procedure described in the preceding section ends with the argon absorbed on a large liquid nitrogen-cooled charcoal trap. The argon is transferred from this absorber to the purification system by heating the charcoal to 200°C and gently flowing helium through the trap. During this transfer, the gas flows through a hot titanium getter and is subsequently collected on a much smaller charcoal trap at the beginning of the gas purification system. The sample is separated from the helium remaining from the transfer procedure by leaving the trap at 77 K (liquid nitrogen temperature), so that the argon remains securely adsorbed to the charcoal, and evacuating the helium. (This procedure is used in several subsequent stages of processing as well.)

Next, we heat the small charcoal trap mentioned above to 200°C and use a Toepler pump to move the evolved gas from that trap to a small, volumetrically calibrated stem. (A Toepler pump is a glass pump filled with mercury that is used to transfer a sample from one place to another by raising and lowering the mercury level.) After volume measurement, the gas is again gettered over hot titanium metal to remove reactive gases and then adsorbed onto another charcoal column at 77 K. This latter column is part of a gas chromatographic system that separates argon from the heavier rare gases, krypton, xenon, and radon.

The argon gas is collected at the output of the chromatography column on another charcoal trap at 77 K, separated from the helium by evacuation, and collected in a second Toepler pump. The volume of the recovered argon gas is measured and mixed with a sufficient volume of air argon to fill the proportional counter to be used to a pressure of 1.2 atm (absolute). This gas is gettered over hot titanium for the third and final time. Finally, the argon sample is adsorbed on a very small charcoal trap at 77 K, and any small amount of helium remaining is pumped off. The charcoal trap is heated to -50°C (this temperature is used to reduce residual Rn in the counter filling), and the argon volume is collected and measured in the Toepler pump. The argon is transferred to the waiting proportional counter. A volume of methane equal to approximately 7% of the argon volume is next taken from a storage bulb and added to the argon in the counter. Finally, mercury is used to push the 93% argon-7% CH<sub>4</sub> mixture into the counter to a preset level, and the total counter pressure is measured. The counter is removed from the vacuum system, its exterior is cleaned with hexane, and it is installed in the counting system.

All volume measurements of gas samples are made on the stem of a Toepler pump by reading the height of the column of mercury that forces the sample into a 3 cm<sup>3</sup> internal stem. The uncertainty in the measurement of a gas sample is determined by the uncertainty in the absolute volume of this stem, about 2.0%, and the reading error of the mercury manometer, about 1.0 mm of Hg.

#### 4.3. Carrier-based Extraction Efficiency

##### 4.3.1. Carrier Operations

For each exposure, the recovery efficiency for the <sup>37</sup>Ar present in the tank is determined by measuring the efficiency with which we recover a small amount of isotopically separated argon gas, the "carrier gas." A precisely measured amount of this carrier gas is introduced into the tank at the beginning of each exposure. The extraction efficiency is the ratio of the amount of isotopically labeled carrier gas that is recovered in the extraction process to the amount of that carrier gas inserted into the tank.

The carrier gas, about 0.1–0.2 cm<sup>3</sup> (at standard temperature and pressure [STP]) of either <sup>36</sup>Ar or <sup>38</sup>Ar, is measured and inserted into the tank using the apparatus shown in Figure 3. A reservoir containing stable, isotopically enriched argon gas is connected to a pipette whose volume has been accurately measured. Once the pipette volume has been evacuated, the valve to the reservoir is opened, the gas is allowed to expand to equilibrium, and the pressure in the reservoir is measured with an attached mercury manometer. The valve is then closed to isolate the pipette and a stream of helium admitted, which flows the carrier sample into the helium gas stream that returns to the tank from the extraction system. There are two such pipette-reservoir systems, one containing <sup>36</sup>Ar (98% isotopic purity) and one containing <sup>38</sup>Ar (95% isotopic purity). We alternate the use of these two isotopes in adjacent runs. For an <sup>36</sup>Ar run, the number of atoms inserted is

$$n_{36} = \frac{P_{36} V_{36} f_{36}}{k T_i}, \quad (1)$$

where  $V_{36}$  is the volume of the <sup>36</sup>Ar pipette,  $P_{36}$  is the pressure measured at the time of insertion,  $f_{36}$  is the iso-

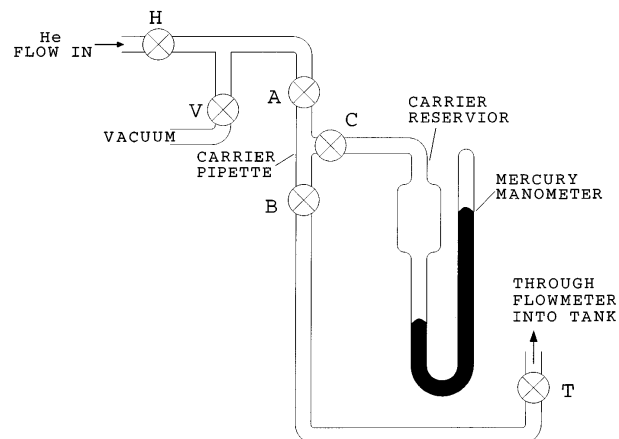


FIG. 3.—Carrier argon measurement and insertion apparatus. This schematic shows the apparatus used to measure and insert a volume of isotopically enriched argon carrier into the C<sub>2</sub>Cl<sub>4</sub> tank, which is used to determine the extraction efficiency (as described in § 4.3). There are two such devices attached to the system, one for <sup>36</sup>Ar and a second for <sup>38</sup>Ar.

topic purity of the reservoir sample, and  $T_i$  is the temperature at the time of the insertion.

Following the insertion, the carrier gas is thoroughly mixed into the tetrachloroethylene for at least 2 hr via the pump-eductor system. During this procedure the gas flow bypasses the extraction system shown in Figure 2. The usual volume of carrier inserted, 0.1 cm<sup>3</sup>, contains  $2.7 \times 10^{18}$  atoms of stable argon. This results in a density of carrier atoms of  $7 \times 10^9$  cm<sup>-3</sup> throughout the detector volume, so that each neutrino-produced  $^{37}\text{Ar}$  atom is just one of many argon atoms at any particular location in the tank.

At the end of the exposure the argon in the tank, both carrier and neutrino produced, is extracted, purified, and put into a proportional counter, as described in the preceding two sections. The volume of the recovered argon gas is measured just before it is inserted into the proportional counter and again, 1 yr later, when the counting period ends and the gas is removed from the counter. These volume measurements are made in the same manner as the measurement of the inserted carrier gas volume, by measuring the pressure produced by the gas in a fixed volume (in this case the stem of the Toepler pump), using a mercury manometer. After being removed from the counter, the gas is sealed into a Pyrex breakseal and transported to a mass spectrometer facility, where the seal is broken and the relative fractions of  $^{40}\text{Ar}$ ,  $^{38}\text{Ar}$ , and  $^{36}\text{Ar}$  are determined.

The number of  $^{36}\text{Ar}$  atoms recovered is given by an expression analogous to that for the number inserted:

$$n'_{36} = \frac{P_T V_T f_{36}^{\text{ms}}}{kT_r} \quad (2)$$

where  $V_T$  is the volume of the Toepler pump stem,  $P_T$  is the pressure measured in the stem of the recovered sample,  $f_{36}^{\text{ms}}$  is the fraction of the gas found to be  $^{36}\text{Ar}$  by the mass spectrometer, and  $T_r$  is the temperature at the time of recovery.

#### 4.3.2. Carrier Analysis

The recovery efficiency for an  $^{36}\text{Ar}$ -based exposure is then just the ratio of the number of  $^{36}\text{Ar}$  atoms recovered ( $n'_{36}$  in eq. [2]) to the number of  $^{36}\text{Ar}$  atoms inserted ( $n_{36}$  in eq. [1]), or

$$\epsilon = \frac{P_T}{P_{36}} \times \frac{V_T}{V_{36}} \times \frac{f_{36}^{\text{ms}}}{f_{36}} \times \frac{T_i}{T_r}. \quad (3)$$

The extraction efficiency thus determined is the first of the three systematic parameters that are needed to convert the number of observed  $^{37}\text{Ar}$  decays into a solar neutrino-induced production rate. The uncertainty in this parameter is determined from the uncertainty in its component measurements. The pressure in the pipette of the initial carrier inserted is determined with a cathetometer and is typically in the range of 150–200 mm of Hg with an uncertainty of 0.5 mm of Hg (0.3%). The pressure of the final recovered sample in the Toepler stem is read from a mercury manometer to a precision of 1.0 mm of Hg on a typical height of 80 mm of Hg (1.3%).

The volumes of the Toepler stem and the carrier pipette enter equation (3) as a ratio, so it is only necessary to determine the relative volume of the two chambers. We do so by directly transferring a gas sample from the carrier pipette to the same Toepler pump that is used for final measurement

of the volume of the extracted argon sample in each run. The uncertainties in absolute measurement then largely cancel, and the total uncertainty in the volume ratio is 2%. Each of the isotopic fractions is determined to 0.5%; samples are taken from the carrier reservoirs and mass-analyzed every 3–5 yr to be confident that there has been no contamination. The temperatures are read to  $\pm 1^\circ\text{C}$ , or about 0.3%. The combination of all these uncertainties results in an overall uncertainty for a single exposure of 2.5%. With the exception of the measurement uncertainty of the volume ratio, all of these measurements are independent from run to run and are added in quadrature for multiple-run analysis.

Since we typically operate the tank extraction system until about 95% of the argon gas in the tank is extracted, each extracted gas sample has both  $^{36}\text{Ar}$  and  $^{38}\text{Ar}$ . The major isotopic component is from the carrier gas put into the detector at the beginning of that exposure and the minor component from the 5% remnant of the carrier of the previous exposure.

The use of a simple ratio between the inserted and recovered amounts of  $^{36}\text{Ar}$  (or  $^{38}\text{Ar}$ ) to determine the recovery efficiency for a particular exposure, as described in the preceding paragraphs, gives a substantially correct first approximation but ignores several subtle (but important) effects. There are several sources that can introduce small amounts of  $^{36}\text{Ar}$  or  $^{38}\text{Ar}$  into the final sample in addition to the carrier sample that was introduced at the beginning of an exposure. These include contributions from the small amount of air argon (0.337%  $^{36}\text{Ar}$ , 0.063%  $^{38}\text{Ar}$ ) that is collected from the tank (or added to the sample to fill the counter to the correct pressure), the fact that the carrier reservoirs have small components of the other isotopes present, and the small residue of the major carrier isotope that remains from the last exposure it was used for, two runs earlier. Each of these effects contributes 1% or less to the final extraction efficiency.

A more complete method of analysis of the carrier recovery information, including treatment of the 5% residue of the dominant isotope of the previous exposure and the small corrections needed for the dominant isotope in the present one, is described in Appendix A. The recovery efficiencies that result from this method typically differ from those produced by the simple analysis described above by not more than 1.5%, with similar errors (~2.5% with variation from run to run). The advantage of the more sophisticated analysis is that by considering both the major isotope for the present exposure and the residue of the other isotope that remains from the previous exposure, we are able to determine separately for each extraction two components of the total recovery efficiency: the efficiency with which argon is extracted from the detector and adsorbed onto the charcoal trap (which can be converted into a gas extraction coefficient for each run) and the efficiency of the gas purification process, that is, the fraction of the gas adsorbed on the charcoal trap that is inserted into the proportional counter.

#### 4.3.3. Run-by-Run Gas Extraction Coefficients

Since the argon solubility equilibrium time constant (driven by 38 eductors) is much less than the total extraction time constant (driven by two eductors), the fraction of argon gas remaining in the tank decreases exponentially with the volume of helium gas,  $h(t)$ , that has passed through

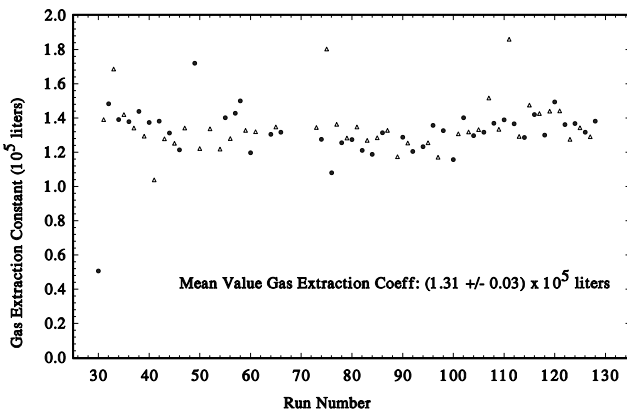


FIG. 4.—Gas extraction coefficients. Value of the extraction constant  $H$ , determined for each run by the method described in Appendix A.

the charcoal trap in time  $t$ , according to:

$$\text{fraction } {}^{37}\text{Ar remaining} = e^{-h(t)/H},$$

where  $H$  is the measured extraction constant. In Figure 4, we show the value of  $H$  for each extraction from the tank, as determined in the carrier analysis described in Appendix A. The reader may note that this plot begins with run 29, rather than the first run in the usual data set, run 18. This is due to the fact that the analysis method that allows the separate determination of  $H$  and the processing efficiency for each run requires the alternate use of  ${}^{36}\text{Ar}$  and  ${}^{38}\text{Ar}$  as the dominant carrier isotope. Runs 18–28 used  ${}^{36}\text{Ar}$  exclusively as the carrier isotope ( ${}^{38}\text{Ar}$  is substantially more expensive, and there was some delay in acquiring it). It is clear from Figure 4 that  $H$  has not varied over the history of the experiment. The best fit to these measurements of  $H$  is  $(1.31 \pm 0.03) \times 10^5$  liters.

#### 4.3.4. Gas Processing Efficiency

The second parameter determined by the carrier recovery measurements is the efficiency of gas recovery from the gas processing system. This consists of a series of purification stages for the gas that has been removed from the charcoal trap, as described above in § 4.2. The gas processing efficiency is the ratio of the volume of recovered gas to the volume of gas introduced into the gas processing system. In Figure 5, we show the measured gas processing efficiency as a function of extraction number. The average value is

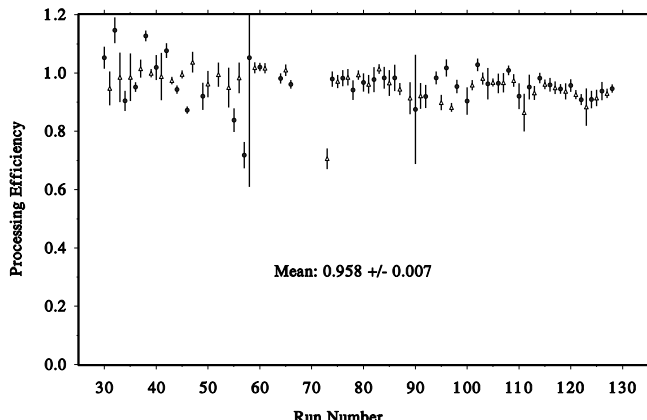


FIG. 5.—Processing efficiency for each extraction, as determined by the method described in Appendix A.

$95.8\% \pm 0.7\%$ . Each of the four runs that show a distinctly low processing efficiency had a clear problem occur in the apparatus during processing. Excluding these four runs, the gas-processing efficiency is essentially the same for all of the extractions (average value 96.8%) and shows no variation with time, an indication of the stability of the apparatus.

#### 4.4. Spatial Uniformity Of Tank Extraction Process

The eductor system was carefully designed to ensure that there would be uniform extraction throughout the tank by swirling the liquid in both the horizontal and vertical planes. The eductors are canted downward at  $45^\circ$  and eject the gas/liquid mixture with sufficient velocity that the plume of bubbles injected into the tetrachloroethylene extends to the walls of the tank. In addition, the eductors are also canted by  $10^\circ$  relative to the axis of the tank, to generate horizontal circulation consistent with the Coriolis effect. The inlet pipe from which the liquid circulation pumps draw tetrachloroethylene extends the length of the tank and is designed to draw fluid uniformly along its length.

The success of these design characteristics was demonstrated by studying the extraction characteristics of the air, 1% of which is argon, that was dissolved in the tetrachloroethylene when it was first put into the tank in the mid-1960s. Clearly, this air argon ( ${}^{40}\text{Ar}$ ) is uniformly distributed throughout the tank.

In Figure 6, we show the differential extraction of the air argon from the detector. Due to the large volume of air argon initially present, it was possible to track the argon recovery yield over 3 orders of magnitude. It is evident that the extraction process is very well described by a single exponential, thus eliminating the possibility that there exist poorly swept regions of the detector. An exponential fit to this extraction curve gives  $H = (1.31 \pm 0.02) \times 10^5$  liters, in excellent agreement with both the measurement of  $H$  determined from the individual exposure carrier yields (given above), as well as measurements made on the extraction rate of internal  ${}^{37}\text{Ar}$  produced via neutron exposure.

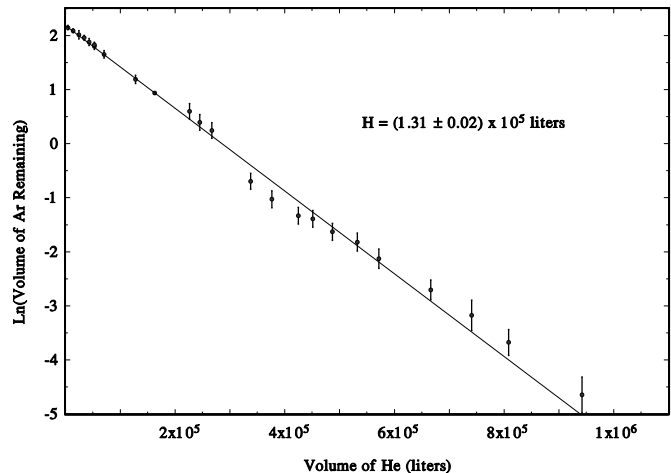


FIG. 6.—Removal of air argon. Amount of air argon remaining in the  $\text{C}_2\text{Cl}_4$  tank as function of the volume of helium that flowed through the system during the initial purge. The response of the system does not deviate from an exponential for over 3 orders of magnitude.

#### 4.5. Chemical Effects

The validity of the use of isotopic carrier as a measure of the recovery efficiency for the experiment depends on the absence of chemical traps that effect only the internally produced argon. It is very unlikely that a rare gas such as argon would be subject to such an effect. Neutrino capture yields an argon ion that has a recoil energy varying from  $\approx 10$  eV for a 861 keV neutrino from  $^7\text{Be}$  to 6 keV for a 14 MeV neutrino from  $^8\text{B}$ . Even at the low end of this range, the  $^{37}\text{Ar}$  ion resulting from neutrino capture has sufficient recoil energy that it will break free of the parent  $\text{C}_2\text{Cl}_4$  molecule. It is generally believed that the ion will then lose energy and exchange charge with a  $\text{C}_2\text{Cl}_4$  molecule, becoming a neutral argon atom. It was, however, suggested (Jacobs 1975) that  $^{37}\text{Ar}$  produced by neutrino capture might not become neutralized or might form a compound, polymer, or molecular ion that would be stable and would not follow the usual chemical behavior of argon gas. This suggestion was based on the observation that some neutral and ionic fragments are produced in mass spectrometer ion sources when argon and  $\text{C}_2\text{Cl}_4$  are present. Measurements, however, show that these compounds will rapidly become neutralized (Leventhal & Friedman 1972; Beulow, Worsnop, & Herschbach 1981) and release the argon atoms.

Nevertheless, a test, using  $^{36}\text{Cl}$ -labeled tetrachloroethylene (half-life of 300,000 yr), was made in a separate apparatus to demonstrate the equivalence of the carrier recovery to that of internally produced argon. The energetics of  $^{36}\text{Cl}$  decay are nearly equivalent to the inverse beta process that yields  $^{37}\text{Ar}$  after neutrino capture in a  $^{37}\text{Cl}$  nucleus: 98% of  $^{36}\text{Cl}$  beta decays into  $^{36}\text{Ar}$ , emitting an antineutrino and an electron with an end-point energy of the electron of 710 keV.

A small volume of  $\text{C}_2\text{Cl}_4$  was specially synthesized with one of the chlorine atoms as  $^{36}\text{Cl}$ . The  $^{36}\text{Cl}$  activity was 7 mCi ( $\approx 0.2$  g of  $^{36}\text{Cl}$ ). The experiment was carried out in a miniature version of the Homestake detector, a 30 liter steel vessel containing 25 liters of  $^{36}\text{Cl}$ -labeled  $\text{C}_2\text{Cl}_4$ . The stable product  $^{36}\text{Ar}$  was removed by helium purge, collected on charcoal, and purified in the usual manner. The recovered gas was neutron activated, converting  $^{36}\text{Ar}$  atoms to  $^{37}\text{Ar}$ . The number of these atoms was then determined by normal  $^{37}\text{Ar}$  counting. Absolute normalization was achieved by simultaneous irradiation of a measured quantity of  $^{36}\text{Ar}$ . The yield of  $^{36}\text{Ar}$ , based upon the known decay rate of  $^{36}\text{Cl}$ , was  $100\% \pm 3\%$  (Bahcall & Davis 1976; Davis 1978; Ruiz & Davis 1978). A similar experiment by others (Gromov et al. 1978) gave a similar result (yield of  $106\% \pm 10\%$ ). These experiments demonstrate that, as expected, the  $^{37}\text{Ar}$  atoms resulting from solar neutrino-induced inverse beta decay behave chemically in exactly the same manner as the many argon carrier atoms found throughout the detector.

Additional details regarding extraction tests can be found in many conference proceedings, especially in Davis (1994b).

#### 5. COUNTING

##### 5.1. $^{37}\text{Ar}$ Decay

The number of  $^{37}\text{Ar}$  atoms extracted from the detector is determined by observing their decay in a miniature gas-filled proportional counter. This type of counter produces a pulse proportional to the charge liberated by an ionizing particle passing through the counter and thus to the energy lost in the counter gas by the ionizing particle.

The specifics of the  $^{37}\text{Ar}$  decay process are shown in Table 2 (Fink 1972). A single-channel, K orbital electron capture with the emission of 3–5 Auger electrons whose total energy is 2.823 keV represents 81.5% of all decays. In addition to being the dominant channel, it is also the easiest channel to detect.

An additional 8.7% of the decays involve a K orbital electron capture together with the emission of an X-ray. From the dimensions of our counters and the conversion probability of the filling gas, primarily argon, we estimate that about 10% of these X-rays are converted and so also give a total energy deposition of 2.8 keV. These decays add another 0.9% to the fraction of decays that deposit 2.8 keV, giving a total of 82.4% of  $^{37}\text{Ar}$  decays in this channel.

#### 5.2. Counter Construction

To observe decays that occur on the order of once per week, it is necessary to devise a counting system whose total rate of background events mimicking  $^{37}\text{Ar}$  decays is much less than one per week. This was achieved by a combination of careful choice of materials of construction for the proportional counters, miniaturization of these counters to reduce the amount of material in the vicinity of the counting region, effective shielding and vetoing of external background signals, and distinct electronic definition of the desired signal. The resultant background count rates are less than one per month.

The proportional counter envelopes (see Fig. 7) are constructed from high-purity fused quartz and have internal volumes of either 0.5 or 0.25 cm<sup>3</sup>. The smaller volume counters have a lower overall background count rate, while the larger counters more effectively reject background events by rise time selection (see the following section), so that the effective background rates for  $^{37}\text{Ar}$  events for the two types are similar. The cathode is a thin-walled hollow cylinder of highly refined iron. A 12–25  $\mu\text{m}$  diameter tungsten wire serves as an anode. The filling gas is pushed up into the counter by a mercury column through a fine capillary that is sealed by a valve, leaving a section of the capillary between the counter and the valve filled with mercury.

TABLE 2  
PRINCIPAL RADIATIONS PRODUCED IN THE DECAY OF  $^{37}\text{Ar}$

Decay Mode	Percent of All Decays	Energy of Auger Electrons (keV)	X-ray (keV)
K .....	81.5	2.823	0.0
L .....	8.9	0.270	0.0
K .....	2.7	0.202	2.621
K .....	5.5	0.201	2.622
M .....	0.9	0.018	0.0
K .....	0.5	0.007	2.816

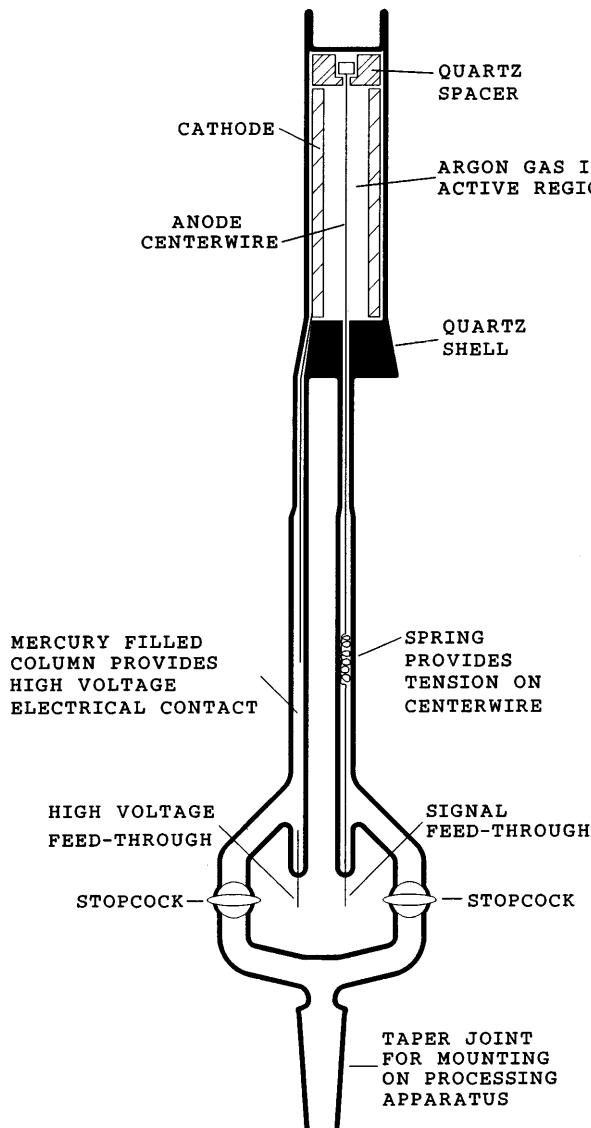


FIG. 7.—Proportional counter geometry. Sketch of the miniature proportional counters used to observe  $^{37}\text{Ar}$  decays. Counters typically have an overall length of 20 cm, with an active region 30 mm long and 4.5 mm in diameter.

This seal assures that no gas is lost by leakage through the valve.

Since the counters are baked out at temperatures in excess of 200°C, a space must be left between the cathode and the counter shell to allow for differential thermal expansion. Decays occurring in this space will not be counted. The effect of this dead space is taken into account when the counters are given their efficiency calibration as described in § 5.4.

### 5.3. $^{37}\text{Ar}$ Counting

The proportional counters are operated inside a large NaI anticoincidence counter, which, in turn, is surrounded by a thick passive shield. The shielding nearest the counters consists of 10 cm of purified mercury. The exterior shielding of one of our counting systems is made from lead bricks while the other counting system has a thick mercury outer shield.

Proportional counters are filled to a pressure of 1.1–1.2 atm. The filling gas is 93% argon, the argon sample

extracted from the tank together with enough additional air argon to fill the counter to the required pressure, and 7% methane. The methane used has been checked to be sure it is very low in tritium.

$^{37}\text{Ar}$  decays in the miniature proportional counters are distinguished from background events by observation of their distinct energy and rise time characteristics. The dominant decay mode of  $^{37}\text{Ar}$ , K orbital electron capture, deposits 2.82 keV of energy in the counting gas in the form of Auger electrons from atomic electron rearrangement. The range of these electrons is very short, less than 100  $\mu\text{m}$ , so that the approximately 100 electron-ion pairs created by the Auger electrons are highly localized. For a given decay all the electrons thus have almost the same drift time to the center wire, resulting in a short rise time charge pulse (less than 5 ns). Background events can arise from a gamma ray interacting with an atom in the counter, usually by Compton scattering; the Compton-scattered electron, if it deposits energy comparable to that of the events we are looking for, will have a range greater than the diameter of the counter and will thus leave ionization distributed over a wide region, leading to a slower rising (10–100 ns) pulse.

The signal from the counter's central anode wire is directly coupled to a fast charge-sensitive preamplifier. The preamplifier output is then split, with one signal going into a standard shaping amplifier (integration time much longer than the pulse rise times) followed by an analog-to-digital converter to measure the pulse energy, and another signal going into a timing filter amplifier to measure the pulse rise time. This timing amplifier differentiates the charge pulse and then integrates the leading edge of the pulse with a short time constant (5 ns). The resultant signal then goes into a pulse stretcher that produces an output signal, called the ADP signal, for "amplitude of the differentiated pulse," which has appropriate rise and fall times for a standard analog-to-digital converter. The ADP signal is thus proportional to energy and inversely proportional to the rise time of the pulse from the proportional counter.

In an ADP versus energy plot,  $^{37}\text{Ar}$  decays occupy a narrow band (Fig. 8), while background events lie in a broad region below this band. Events from electronic noise,

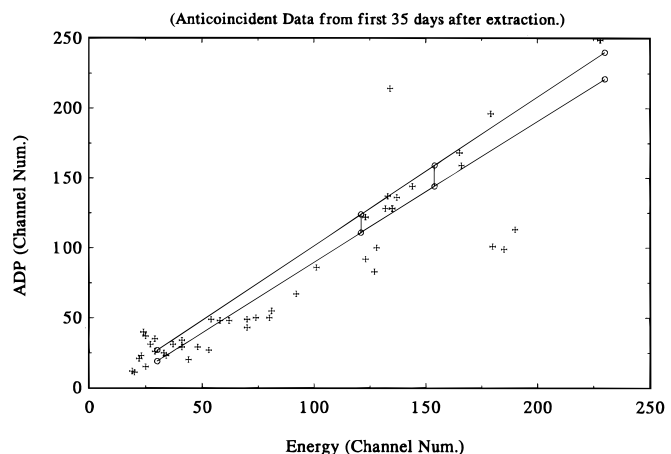


FIG. 8.—ADP vs. energy. (Energy, ADP) of each of the nonvetoed pulses of run 130 that occurred during the first 35 days of counting, together with the energy and ADP bounds of the acceptance region determined by the  $^{55}\text{Fe}$  calibration. The diagonal lines mark the fast region; the vertical lines indicate the one FWHM region about the 2.82 keV energy of the  $^{37}\text{Ar}$  decay.

such as those produced by high-voltage breakdown, have very short rise times and so lie above the fast ADP region. Figure 8 shows a plot of a typical run with a sample taken from the tank after a 2 month exposure. Details of event selection are discussed in § 7.2.

Counters are periodically calibrated with an external source of low-energy X-rays through a thin end or side window in the quartz envelope. Mn X-rays with energy of 5.92 keV emitted by an  $^{55}\text{Fe}$  source are used to calibrate both energy and ADP. In addition to the full-energy peak, they also produce an escape peak at 2.93 keV that occurs when the X-ray leaves a vacancy in the argon K shell and the K X-ray that follows is not detected. This leaves a very small cloud of ionization with a total energy deposition of 2.93 keV, very close to that from  $^{37}\text{Ar}$  decay, which is used to set the energy scale. The fast rise time region in the energy-ADP plot lies between two straight lines that contain 95% of the fast events. These lines are set by taking ADP spectra at four fixed energies, two above and two below the  $^{37}\text{Ar}$  peak, finding the ADP values that include 95% of the events in each spectrum, and then fitting straight lines through these energy-ADP pairs. The expected width of the  $^{37}\text{Ar}$  peak is calculated by inverse square root of energy scaling from the measured resolution at 5.9 keV.

As will be explained in § 7.2, we have established that the neutrino capture rates calculated from the data are not significantly affected by even large changes in the energy and ADP acceptance regions.

The rejection efficiency of slower pulses from Compton electrons is easily determined by using an external gamma source such as  $^{60}\text{Co}$  or by using gamma radiation from environmental background. We typically obtain rejection of 95% of these events in the  $^{37}\text{Ar}$  region. The efficiency of rejection of gamma rays by the NaI anticoincidence detector is 80%–85%.

The system is very stable. Calibrations are carried out every 2 months. During the first few days of operation there may be drifts in energy of several percent. After that time the energy calibration rarely changes by more than 2% over the remaining year of counting. This system and the recording system described below were designed by V. Radeka, R. Chase, and L. Rogers of Brookhaven National Laboratory (Davis et al. 1972). It has functioned with remarkable reliability for 25 years.

Information on each event was originally recorded on punched tape. For many years now it has been recorded by computers in the mine, which are regularly read over the telephone lines from Philadelphia.

The information recording system is triggered by a pulse from the ADP amplifier that exceeds a level well below that expected for an  $^{37}\text{Ar}$  decay. For each event, the following information is recorded:

1. The amplitude of the pulse from the NaI(Tl) veto counter.
2. The energy and ADP of the event.
3. The energy and ADP of two test pulses, simulating fast events with energy above and below the energy of expected  $^{37}\text{Ar}$  events, generated immediately after each event. This keeps a running check on the operation of the energy and ADP recording systems.
4. The difference in time between the peaks of the energy and ADP pulses. This is a check that the ADP system has indeed recorded a pulse of normal shape.

5. A scaler giving the number of trigger pulses recorded. This gives an indication of any noise in the system that might lead to dead time.

6. The date and time of the event.

The counting was originally done at the surface of the Earth, at Brookhaven National Laboratory. In 1977 the counting was moved to its present site underground next to the solar neutrino detector. This reduced the background due to cosmic ray muons. Each sample is counted for 250–400 days.

#### 5.4. Counter Efficiency Calibration With $^{37}\text{Ar}$

The second parameter that is needed to convert the observed number of  $^{37}\text{Ar}$  decays into a solar neutrino-induced production rate is the efficiency for observing such decays in the proportional counter. This efficiency is determined by filling each counter with a known amount of  $^{37}\text{Ar}$ , typically  $10^7$ – $10^8$  atoms (giving a decay rate of  $\sim 100 \text{ s}^{-1}$ ). The fraction of  $^{37}\text{Ar}$  decays actually observed in the miniature counter that fall within a given energy and ADP acceptance window then directly determines the counter efficiency for that window. Figure 9a shows a typical pulse height distribution of  $^{37}\text{Ar}$  decays in a counter being calibrated. The low-energy tail below the main peak represents decays that occur near the ends of the cathode, where the fringing electric fields result in reduced gain.

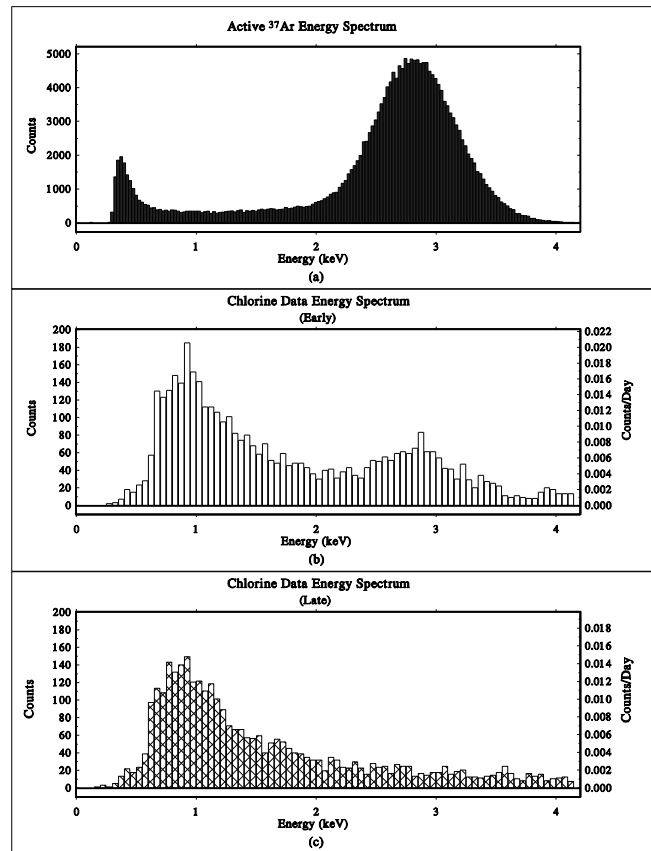


FIG. 9.—(a) Energy spectrum from a counter filled with active  $^{37}\text{Ar}$ . (b) Cumulative energy spectrum from 93 solar neutrino observations (early counting data: 0–105 days following the end of an extraction). (c) Cumulative energy spectrum from 93 solar neutrino observations (late counting data: 175–350 days following the end of an extraction). Plots (b) and (c) are of events with normalized ADP between 0.85 and 1.02 (i.e., fast events).

The absolute  $^{37}\text{Ar}$  decay rate of the calibration gas fill is measured in a specially designed counter, with a large and very well-known active volume, in which the cathode is chemically deposited onto the quartz envelope to eliminate dead gas regions behind the cathode. Special provisions are also made to avoid cathode end effects. The relative uncertainty in the efficiency of a miniature proportional counter as determined by this direct method is 2.5%. For a detailed discussion of the procedure used in experimentally calibrating counters, see Appendix B.

From the geometric dimensions of the counter components, we have also modeled the counter response and calculated the counter efficiency. This mathematical prediction of the counter efficiency is in very good agreement with that determined experimentally. Unfortunately, some counters used in the experiment were broken before direct calibrations using  $^{37}\text{Ar}$  could be carried out. For these counters, we have used the counter efficiency predicted by the model. The relative uncertainty used for these counters is 5%, determined by the level of agreement between the  $^{37}\text{Ar}$  calibrations and the model calculations for counters that have been directly calibrated.

## 6. NONSOLAR PRODUCTION OF $^{37}\text{Ar}$

The extraction efficiency and counting efficiency described in the previous two sections allow us to convert an observed number of  $^{37}\text{Ar}$  decays into a total  $^{37}\text{Ar}$  production rate in the  $\text{C}_2\text{Cl}_4$  tank. To finally determine the solar neutrino-induced  $^{37}\text{Ar}$  production rate, we must subtract from the total rate the rate of  $^{37}\text{Ar}$  production from all nonsolar neutrino sources. We consider below the production of  $^{37}\text{Ar}$  in the detector by three such sources: cosmic rays, local radioactivity external to the tank, and radioactivity within the tank. A large number of other possible sources of  $^{37}\text{Ar}$ , such as the inleakage of  $^{37}\text{Ar}$  from the atmosphere, production by  $\alpha$ -particle emitters via the reaction  $^{34}\text{S}(\alpha, n)^{37}\text{Ar}$ , production by cosmic-ray neutrinos, etc., can be shown to be insignificant.

### 6.1. Cosmic Rays

The largest source of nonsolar production for the  $^{37}\text{Cl}\text{-}^{37}\text{Ar}$  experiment is the production of  $^{37}\text{Ar}$  by the photonuclear interaction of energetic muons. At the depth of the detector,  $4200 \pm 100$  m.w.e., the average muon energy is 300 GeV, with a total intensity of  $\sim 4$  muons  $\text{m}^{-2} \text{ day}^{-1}$ . These muons lose energy by photonuclear interactions with nuclei, producing light evaporation products such as protons, neutrons, tritons,  $^3\text{He}$ , and other strongly interacting particles, mostly pions. The primary and secondary protons resulting from these interactions produce the principal nonsolar signal in the chlorine experiment via  $^{37}\text{Cl}(p, n)^{37}\text{Ar}$ .

The production rate from these energetic muons was initially determined by a direct depth-intensity measurement of the rate of  $^{37}\text{Ar}$  production in tetrachloroethylene detectors. Measurements of the  $^{37}\text{Ar}$  production rate in 6800 liters of  $\text{C}_2\text{Cl}_4$  in movable tank cars were made at four depths in the Homestake mine, the deepest of which was 1800 m.w.e. This production rate was then extended to the depth of the solar neutrino detector by scaling with a power of the muon energy and the muon flux (Wolfendale, Young, & Davis 1972; Cassidy 1973; Zatsepin et al. 1980).

Since this direct measurement requires a substantial extrapolation from the final measurement point to the

depth of the detector (4200 m.w.e), a more sensitive detector observing the direct reactions  $^{39}\text{K}(\mu, \mu 2n)^{37}\text{K} \rightarrow ^{37}\text{Ar}$  and  $^{39}\text{K}(\mu, \mu pn)^{37}\text{Ar}$  was suggested by Fireman (Spannagel & Fireman 1972; Fireman et al. 1985). Such measurements were initiated in 1984, using four separate tanks, each containing 1 metric ton of potassium. Two of the tanks were mobile and were used to determine the  $^{37}\text{Ar}$  production rate at higher levels of the mine, while the other two were fixed in the solar neutrino chamber. All four tanks were used to measure the  $^{37}\text{Ar}$  production rate at the depth of the solar neutrino detector.

The depth dependence for  $^{37}\text{Ar}$  production from  $^{37}\text{Cl}$  and  $^{39}\text{K}$  is expected to be proportional to both the muon flux  $\phi_\mu$  and a power of the average muon energy  $m$ ,  $\langle E_\mu \rangle^m$ , where  $m \approx 0.7$  (Ryazhskaya & Zatsepin 1965; Ryazhskaya 1991). Since the production process in tetrachloroethylene results from a muon secondary and the process in potassium is due to direct muon interaction, there is no a priori reason to expect that the energy dependence exponent  $m$  of the two processes will be identical. However, fits to the production rates from both isotopes indicate that the exponent is in fact the same for both processes, within errors. Thus, the  $^{39}\text{K}$  measurements both validate the general scaling procedure used and can be used to directly scale the  $^{37}\text{Ar}$  production from  $^{37}\text{Cl}$  at the depth of the Homestake chamber from the  $^{39}\text{K}$  measurement at that depth. The cosmic-ray contribution to the  $^{37}\text{Ar}$  production rate, determined using the information from both the  $\text{C}_2\text{Cl}_4$  and the  $^{39}\text{K}$  depth-intensity curves, is  $0.047 \pm 0.013$  atoms  $\text{day}^{-1}$  (Cleveland et al. 1998).

### 6.2. Neutrons From the Rock Wall

Next, we evaluate the  $^{37}\text{Ar}$  production rate due to fast neutrons from the surrounding rock walls. Neutrons are produced in all rocks by  $\alpha$ -particle emitters of the uranium and thorium series by  $(\alpha, n)$  reactions on light nuclei and from the spontaneous fission of  $^{238}\text{U}$ . The energetic neutrons produce  $^{37}\text{Ar}$  in the detector liquid by the reaction sequence  $^{35}\text{Cl}(n, p)^{35}\text{S}$ , followed by  $^{37}\text{Cl}(p, n)^{37}\text{Ar}$ . The neutron energy threshold for this process is 1.0 MeV. Such neutrons are easily eliminated by a modest water shield, one that was provided for in the design of the detector.

The fast neutron flux in the tank room was measured radiochemically by the reaction  $^{40}\text{Ca}(n, \alpha)^{37}\text{Ar}$ , where the calcium was in the form of a solution of calcium nitrate. The  $^{37}\text{Ar}$  was recovered by a helium purge, collected, purified, and counted in a proportional counter. The relative  $^{37}\text{Ar}$  yield per neutron from Ca in the calcium nitrate detector (a  $60 \times 90 \times 10$  cm thick tank filled with a concentrated  $\text{Ca}[\text{NO}_3]_2$  solution) to Cl in the  $\text{C}_2\text{Cl}_4$  tank was measured to be 4100. This response ratio was determined by exposing the  $\text{Ca}(\text{NO}_3)_2$  detector to an external Pu-Be source and then placing this same source at the center of a large tank filled with  $\text{C}_2\text{Cl}_4$ . The spectrum of neutrons from a Pu-Be source is a reasonable approximation to the neutron spectrum from the Homestake rock as 90% of the fast neutron flux in the Homestake chamber is due to  $(\alpha, n)$  reactions on light nuclei (Barabanov et al. 1983).

Measurements with calcium nitrate detectors of the size given above were made in five locations in the Homestake chamber prior to the installation of the  $\text{C}_2\text{Cl}_4$  tank. After scaling by the relative yield for  $\text{Ca}(\text{NO}_3)_2$  and  $\text{C}_2\text{Cl}_4$  (as described above) and the surface area of the respective tanks, these measurements indicate a production rate in the

large tank due to fast neutrons of  $0.05 \pm 0.025$   $^{37}\text{Ar}$  atoms day $^{-1}$ , when there is no external shielding. The tank chamber may be flooded to produce a water shield at least 1 m thick in all directions. In this configuration, all neutrons are assumed to be moderated, so that their contribution to the production rate is less than  $0.002$   $^{37}\text{Ar}$  atoms day $^{-1}$ . In 1984, the water shield was removed and the tank surrounded by a 30 cm thick shield of liquid scintillator. This shield reduces the fast neutron-induced production to  $0.03 \pm 0.025$   $^{37}\text{Ar}$  atoms day $^{-1}$ . (No data from the liquid scintillation detector has been used in the determination of the nonsolar  $^{37}\text{Ar}$  production rate.) Due to the variable nature of the nonsolar production rate, the results presented in this paper represent neutrino-induced production rates only, where the rate of nonsolar  $^{37}\text{Ar}$  production has already been subtracted on a run-by-run basis.

### 6.3. Internal $\alpha$ -Particles

Alpha particles arising from radioactive contaminants in the tank or tetrachloroethylene may produce  $^{37}\text{Ar}$  via  $(\alpha, p)$  reactions followed by  $(p, n)$  on  $^{37}\text{Cl}$ . The  $\alpha$ -particle activity of all the components of the detector was carefully monitored during the construction phase. The steel to be used for the tank was tested for surface  $\alpha$ -particle activity before fabrication of the parts to ensure it would meet the experimental requirements. The underground welding of the tank was performed with unthoriated welding rod and flux to eliminate a possible source of contamination. Before the tank was filled, the inner surface was cleaned by shot-blasting (with steel shot), vacuumed, and wiped down with solvent. The surface  $\alpha$ -particle emission of the clean walls was then measured in four locations with a windowless  $60 \times 180$  cm multiwire proportional counter designed to fit the curved walls of the tank. All piping was cleaned with acid at the plant and the ends sealed. On arrival at Homestake, the  $\alpha$ -particle activity of the inner surface of each pipe was measured by converting it into a large proportional counter before installation of the plumbing. Samples of  $\text{C}_2\text{Cl}_4$  from each of the 10 tank cars used to ship the tetrachloroethylene were evaporated to dryness and the residue counted under a windowless  $\alpha$ -particle counter. This assay was performed on each tank car both at the production facility in Wichita, Kansas and on arrival at Homestake.

The cumulative rate of  $\alpha$ -particle emission into the  $\text{C}_2\text{Cl}_4$  was determined from these tests to be less than  $10^8$   $\alpha$ -particles day $^{-1}$  (Davis 1978). The  $^{37}\text{Ar}$  yield per incident  $\alpha$ -particle was determined by dissolving an assayed sample of  $^{222}\text{Rn}$  in a flask of  $\text{C}_2\text{Cl}_4$ . The resulting  $^{37}\text{Ar}$  atoms were removed and counted in the usual manner. The yield measured in this experiment was  $1.7 \times 10^{-10}$   $^{37}\text{Ar}$  atoms per  $^{222}\text{Rn}$  decay, which includes three consecutive  $\alpha$ -particle decays of 5.5, 6.0, and 7.7 MeV. Since the spectrum of  $\alpha$ -particles in the vessel is unknown, as a generous estimate we can use this as the yield of a single  $\alpha$ -particle to determine an upper limit on  $^{37}\text{Ar}$  production due to  $\alpha$ -particle emission of  $0.017$  atoms day $^{-1}$ .

### 6.4. Atmospheric Neutrinos

The production of  $^{37}\text{Ar}$  in our detector due to neutrinos ( $\nu_e$  and  $\nu_\mu$ ) produced in the Earth's atmosphere can be determined from calculations of the flux, the spectrum, and the interaction cross section. The most recent calculations indicate that this source makes a virtually negligible contribution to the nonsolar production rate:  $0.42 \times 10^{-3}$  atoms

day $^{-1}$  (Domogatskii & Eramzhyan 1977),  $1.2 \times 10^{-3}$  atoms day $^{-1}$  (Rudzskii & Seidov 1979), and  $0.3 \times 10^{-3}$  atoms day $^{-1}$  (Gaisser & Stanev 1985).

## 7. ANALYSIS AND RESULTS

### 7.1. Introduction

Our standard data set consists of 108 solar neutrino observations made between 1970 and 1994. There are two subsets of the data that merit special consideration. The first seven runs in the standard data set used slightly different electronics, resulting in a narrower ADP response than that of the remaining runs. Hence, although the same analysis techniques are applied to these seven runs, it is not appropriate to include their events in ADP plots made using the bulk of the data. In addition, eight of the remaining 101 runs display excessively high background rates. Their average background is about a factor of 4 times higher than the average background for the other 93 runs, giving cumulative spectra a misleading appearance if they are included. In order to give the reader a clear picture of the bulk of the data, the energy, ADP, and time-rate plots that appear in this paper have been made using only the data from the 93 runs that have consistent electronic response and consistently low backgrounds. The remaining 15 runs are appropriately included in the final analysis.

### 7.2. Event Selection

Orbital K capture results in the emission of 3–5 Auger electrons depositing 2.82 keV of energy in the counter. As discussed earlier, by combining energy (pulse height) with ionization localization (pulse rise time), it is possible to reject most background triggers and select a clean  $^{37}\text{Ar}$  decay sample.

Since  $^{37}\text{Ar}$  has a half-life of 35 days, most (87.5%) of the atoms will have decayed within 105 days (three half-lives) after the extraction from the tank. Once 175 days (five half-lives) have elapsed, only  $\sim 3\%$  of the  $^{37}\text{Ar}$  atoms remain in the counter. Spectra of the events selected as  $^{37}\text{Ar}$  candidates in the first 105 days thus represent a combination of signal plus background and can be compared against spectra made with candidate events from after 175 days, which are virtually all background.

Figure 9 shows the energy spectra given by (a) a counter filled with active  $^{37}\text{Ar}$ ; (b) combined data from 93 solar neutrino runs in the first 105 days following extraction (signal + background); and (c) data from the same set of runs following counting day 175 (background only). If we subtract the later data from the early data (after appropriate normalization for counting live time), the resultant spectrum fits well to a Gaussian, with maximum at 2.85 keV and resolution of 27.5%. This peak energy is in very good agreement with the expected value of 2.82 keV, and the resolution is only slightly larger than 26% predicted from the typical measured resolution of 17%–19% for the  $^{55}\text{Fe}$  peak at 5.92 keV.

Since the ADP value of an event is dependent on both its energy and the characteristics of the proportional counter and gas fill used, it is not possible to directly construct a single cumulative ADP plot for events over a range of energies or that occur in different counters. We have defined a normalized ADP that is energy- and counter-independent and thus permits such a cumulative plot. The normalized value of the ADP for a given event is defined by the

equation:

$$\text{normalized ADP} = 1 - \left( \frac{U - \text{ADP}}{U - L} \times 0.1 \right),$$

where  $U$  and  $L$  represent the upper and lower limits of the "fast" region at the energy of the event (as defined by the  $^{55}\text{Fe}$  calibration; see Fig. 8 and § 5.3). This normalization gives any event that falls on the upper edge of the fast region a value of 1.0 and any event that falls on the lower edge a value of 0.9. Figures 10a–10c show normalized ADP spectra for the same data sets as Figure 9. The characteristic fast signal of  $^{37}\text{Ar}$  decays can clearly be seen in the comparison of the early data to the later data.

The events to be used in the maximum likelihood time series analysis (discussed in the next section) are selected by making cuts in both the energy and ADP spectra. These cuts can either be characterized as "tight," when relatively small regions in the energy or ADP distributions are chosen, or "loose," when larger bounds are allowed. Tight cuts have the advantage of increasing the signal-to-background ratio for the events selected but can also result in larger contributions to the uncertainties in the selection efficiency, due to the fact that the efficiency changes appreciably with window aperture. Making a looser cut reduces the signal-to-background ratio but also reduces the uncertainty in the selection efficiency, as changes in the size of the acceptance window in these regions result in only very small

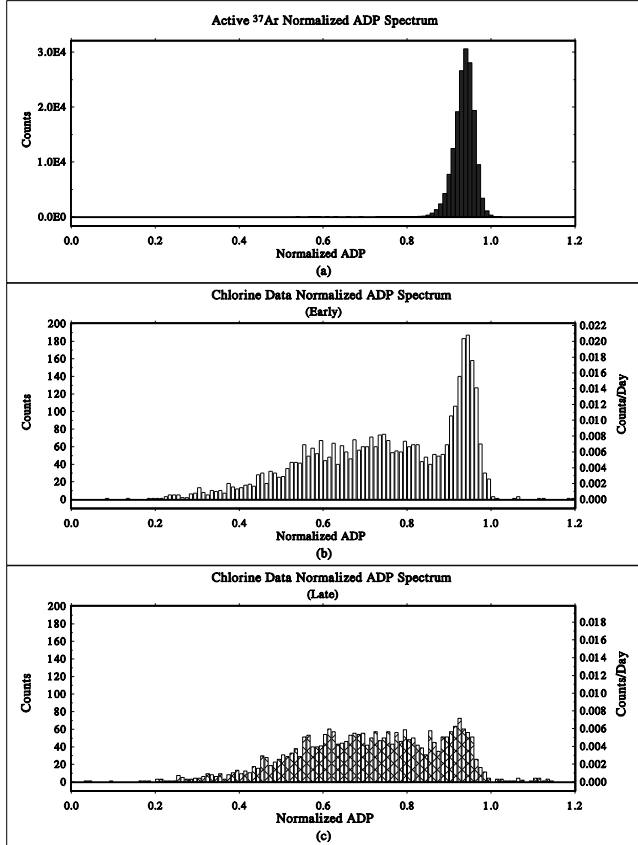


FIG. 10.—(a) ADP spectrum from a counter filled with active  $^{37}\text{Ar}$ . (b) Cumulative ADP spectrum from 93 solar neutrino observations (early counting data: 0–105 days following the end of an extraction). (c) Cumulative ADP spectrum from 93 solar neutrino observations (late counting data: 175–350 days following the end of an extraction). Plots (b) and (c) are of events with energy between 2.0 and 3.6 keV.

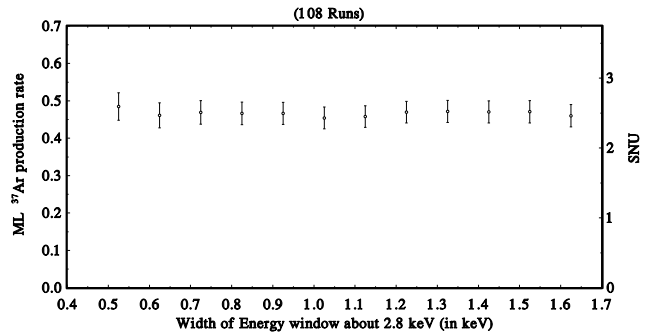


FIG. 11.—Results: variable energy selection. Average SNU rate for the Homestake detector, as a function of the width (about 2.8 keV) of the energy acceptance region for  $^{37}\text{Ar}$  events in the proportional counter. The smallest acceptance region runs from 2.55 to 3.05 keV (0.5 keV width); the largest is from 2.0 to 3.6 keV (1.6 keV width) (see Fig. 9).

changes in the selection efficiency. Since the statistical error for a single run is very large, in the analysis of individual runs we have always chosen to maximize the signal-to-background ratio by making relatively tight cuts: one FWHM about the centroid in energy ( $\sim 2.4\text{--}3.2$  keV;  $\sim 66\%$   $^{37}\text{Ar}$  acceptance) and at 0.9 in normalized ADP ( $\sim 90\%$   $^{37}\text{Ar}$  acceptance). The systematic error due to selection effects for these cuts for a single run is in the range of 5%–10%, much smaller than the statistical error.

In the combined analysis of many runs, the statistical error on the cumulative result drops significantly, making it desirable to relax the selection process and thereby reduce the systematic uncertainty. The largest useful selection region is between 2.0 and 3.6 keV in energy ( $\sim$  two FWHM;  $\sim 88\%$   $^{37}\text{Ar}$  acceptance) and between 0.83 and 1.02 in normalized ADP ( $\sim 99.9\%$   $^{37}\text{Ar}$  acceptance). This ADP window rejects virtually no  $^{37}\text{Ar}$  events, and less than 0.5% of  $^{37}\text{Ar}$  counts have energies above 3.6 keV. The 12% of events rejected by this energy cut are in the degraded event tail and can only be included at the expense of also including the rapidly increasing low-energy background. Use of this selection region reduces the systematic uncertainty due to selection effects to the range of 1%–2%.

A convenient means of testing the selection efficiency is to calculate the result as a function of selection window. Figures 11 and 12 show the cumulative result for 108 runs using a variable selection region in energy (Fig. 11) and ADP (Fig. 12). The energy selection window is a symmetri-

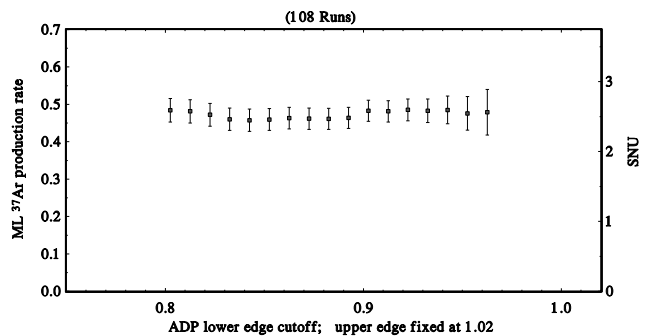


FIG. 12.—Results: variable ADP selection. Average SNU rate for the Homestake detector, as a function of the low edge of the normalized ADP acceptance region; the high edge is fixed at 1.02 (see Fig. 10).

cal region centered about 2.8 keV, whose width is plotted on the  $x$ -axis: 0.5 keV indicates a window from 2.55 to 3.05 keV ( $\sim 53\%$  acceptance), while a width of 1.6 keV is the window from 2.0 to 3.6 keV described above ( $\sim 88\%$  acceptance). The ADP window has a fixed upper edge at 1.02 on the normalized ADP plot and a lower edge that ranges from 0.79 ( $\sim 100\%$  acceptance) to 0.96 ( $\sim 20\%$  acceptance). The  $^{37}\text{Ar}$  production rate is clearly stable over a wide range of selection windows in both parameters.

### 7.3. Data Analysis

The result of the event selection process described in the previous section is a time series of events that all fit the criteria for  $^{37}\text{Ar}$  decays. Using this time series, a fit is made to a decaying exponential with a half-life fixed at 35 days (the  $^{37}\text{Ar}$  signal) plus a decaying background whose half-life can be varied. In earlier analyses, this background has been assumed to be constant in time ( $\tau_{1/2} = \infty$ ) since there were too few background counts in any single run to obtain any useful information concerning the nature of the background. However, analysis of the background in the cumulative data set indicates that these events can be better characterized as occurring with a half-life in the range of 2–3 yr. A time-rate plot for the slow data in the  $^{37}\text{Ar}$  region (energy = 2.0–3.6 keV; ADP = 0.4–0.8) clearly indicates a finite half-life for the background. Several counters have been used for a number of runs over 5–7 yr intervals, allowing the counter background rate to be tracked over an extended time period. These observations of specific counters also display a background that drops off with time. In both the cumulative time-rate plot and in individual counters, the half-life observed is consistent with a time constant,  $\tau_{1/2} = 2.7$  yr. Noting that the half-life of  $^{55}\text{Fe}$  is 2.7 yr and that 96 out of 108 runs have been counted using iron cathodes, we have assumed a 2.7 yr half-life for the background in the present analysis.

The results of the fit are two parameters, a production rate,  $p$ , of  $^{37}\text{Ar}$  in the detector, and an initial background rate,  $b$ , of false events generated in the counter. If we assume a constant rate of  $^{37}\text{Ar}$  production in the  $\text{C}_2\text{Cl}_4$  during the exposure and a decaying background rate in the counter with  $\tau_b = 2.7$  yr, then the probability for producing the particular time series of events which we observe is given by the expression

$$\mathcal{P}(t_1 \dots t_n | p, b) \propto e^{-(N_b + N_c)} \prod_{i=1}^n (be^{-\lambda_b t_i} + p\epsilon_e \epsilon_c S e^{-\lambda t_i}) \\ \equiv \mathcal{L}(\text{the likelihood function}),$$

where

$n$  = total number of candidate  $^{37}\text{Ar}$  events ,

$t_i$  = time of  $i$ th candidate  $^{37}\text{Ar}$  event ,

$\lambda = ^{37}\text{Ar}$  decay constant (35.04 days) ,

$\lambda_b$  = background decay constant (2.7 yr) ,

$\epsilon_e$  = extraction efficiency ,

$\epsilon_c$  = counting efficiency ,

$S = 1 - e^{-\lambda t_{\text{exp}}}$ , the saturation fraction ,

$t_{\text{exp}}$  = exposure time of tank ,

$$\Delta = \sum_{k=1}^m (e^{-\lambda t_{\text{bk}}} - e^{-\lambda t_{\text{ek}}})$$

(probability that an  $^{37}\text{Ar}$  atom that is extracted will decay at a time when it could be counted),

$t_{\text{bk}}, t_{\text{ek}}$  = beginning and ending time of  $k$ th counting interval ,

$m$  = total number of counting intervals ,

$$N_b = \frac{b}{\lambda_b} \sum_{k=1}^m (e^{-\lambda_b t_{\text{bk}}} - e^{-\lambda_b t_{\text{ek}}}) ,$$

(effective number of observed background events), and

$$N_c = p\epsilon_e \epsilon_c S \Delta / \lambda$$

(effective number of observed  $^{37}\text{Ar}$  atoms. The reader is reminded that  $\Delta = 1$  [100% “ON time”] was assumed for the expression used in § 3.2.)

The method of maximum likelihood (Cleveland 1983; Opendak & Wildenhain 1992) is used to determine the pair of parameters  $p$  and  $b$  that has the highest probability of producing the observed sequence of events in the counter (and thus maximizes the likelihood function). The fit includes explicitly a correction for the nonsolar production of  $^{37}\text{Ar}$  in the detector, which has varied somewhat during the overall observing period (due to variations in the shielding arrangements) and takes into account the  $\pm 3\%$  change in the production rate due to the eccentricity of the Earth’s orbit. The final result is thus a production rate of  $^{37}\text{Ar}$  that may be ascribed to the flux of neutrinos from the Sun at the average Earth-Sun distance. Table 3 gives the results of the 108 completed solar neutrino observations. We should note that for purposes of historical continuity, the individual results presented here have been analyzed by selecting events within the “tight” windows described earlier (one FWHM for energy and 0.9–1.0 for ADP), and using the traditional assumption that  $\tau_b = \infty$ . (To convert production rates into SNUs, multiply by 5.35.) The 108 completed solar neutrino observations are plotted in Figure 13.

The method of maximum likelihood is also used to combine the results of all 108 observations to find the production rate that is most likely to have produced the entire data set. The average production rate for several runs is found by multiplying the likelihood functions of these runs together and searching parameter space for the most likely

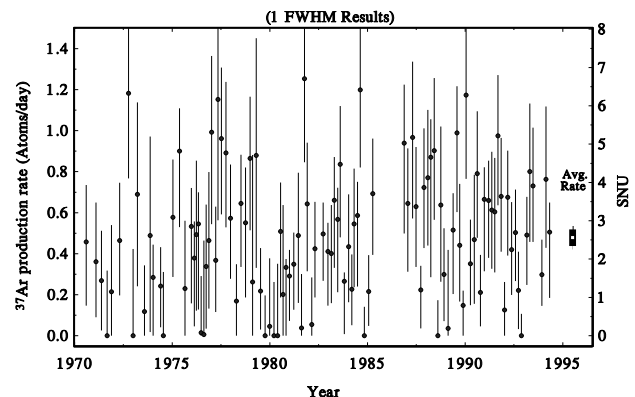


FIG. 13.—Homestake Experiment—one FWHM results. Results for 108 individual solar neutrino observations made with the Homestake chlorine detector. The production rate of  $^{37}\text{Ar}$  shown has already had all known sources of nonsolar  $^{37}\text{Ar}$  production subtracted from it. The errors shown for individual measurements are statistical errors only and are significantly non-Gaussian for results near zero. The error shown for the cumulative result is the combination of the statistical and systematic errors in quadrature.

TABLE 3  
HOMESTAKE RESULTS USING ONE FWHM ANALYSIS

RUN	EXPOSURE TIMES			$^{37}\text{Ar}$ PRODUCED PER DAY			COUNTER BACKGROUND PER DAY		
	Start	Stop	Mean	Best Fit	68% Confidence Range		Best Fit	68% Confidence Range	
18.....	1970.281	1970.873	1970.779	0.457	0.147	0.735	0.043	0.016	0.070
19.....	1970.873	1971.180	1971.098	0.361	0.090	0.649	0.116	0.089	0.143
20.....	1971.180	1971.462	1971.383	0.269	0.025	0.512	0.037	0.020	0.055
21.....	1971.462	1971.755	1971.675	0.000	0.000	0.317	0.050	0.022	0.078
22.....	1971.755	1971.953	1971.887	0.214	0.000	0.540	0.048	0.006	0.090
24.....	1972.171	1972.379	1972.311	0.464	0.197	0.746	0.016	0.006	0.027
27.....	1972.519	1972.849	1972.765	1.182	0.767	1.569	0.038	0.016	0.060
28.....	1972.849	1973.073	1973.002	0.000	0.000	0.423	0.088	0.000	0.292
29.....	1973.073	1973.287	1973.218	0.689	0.241	1.138	0.049	0.025	0.072
30.....	1973.287	1973.668	1973.581	0.118	0.000	0.343	0.035	0.019	0.051
31.....	1973.668	1973.953	1973.873	0.488	0.018	0.971	0.098	0.060	0.137
32.....	1973.953	1974.070	1974.023	0.284	0.000	0.444	0.000	0.000	0.075
33.....	1974.070	1974.487	1974.398	0.242	0.041	0.432	0.020	0.005	0.035
35.....	1974.500	1974.591	1974.553	0.000	0.000	0.311	0.028	0.014	0.043
36.....	1974.591	1975.122	1975.029	0.577	0.286	0.859	0.027	0.013	0.040
37.....	1975.122	1975.454	1975.370	0.900	0.530	1.109	0.000	0.000	0.029
38.....	1975.454	1975.733	1975.655	0.230	0.000	0.561	0.059	0.000	0.121
39.....	1975.733	1976.062	1975.978	0.533	0.158	0.721	0.016	0.000	0.044
40.....	1976.065	1976.179	1976.134	0.379	0.045	0.557	0.008	0.000	0.023
41.....	1976.179	1976.270	1976.232	0.493	0.122	0.854	0.021	0.007	0.035
42.....	1976.270	1976.385	1976.339	0.545	0.128	0.700	0.000	0.000	0.091
43.....	1976.385	1976.540	1976.483	0.014	0.000	0.291	0.030	0.013	0.048
44.....	1976.540	1976.674	1976.623	0.006	0.000	0.464	0.039	0.018	0.060
45.....	1976.674	1976.770	1976.730	0.337	0.034	0.639	0.019	0.005	0.033
46.....	1976.770	1976.922	1976.866	0.464	0.132	0.798	0.044	0.024	0.064
47.....	1976.922	1977.073	1977.017	0.993	0.544	1.365	0.022	0.003	0.042
48.....	1977.073	1977.286	1977.217	0.368	0.115	0.629	0.031	0.014	0.049
49.....	1977.286	1977.381	1977.342	1.152	0.563	1.577	0.010	0.000	0.024
50.....	1977.381	1977.590	1977.521	0.962	0.592	1.308	0.009	0.002	0.017
51.....	1977.590	1977.822	1977.750	0.892	0.529	1.238	0.019	0.009	0.030
52.....	1977.824	1978.055	1977.984	0.573	0.278	0.835	0.009	0.001	0.018
53.....	1978.055	1978.361	1978.280	0.169	0.000	0.349	0.030	0.016	0.044
54.....	1978.361	1978.596	1978.523	0.645	0.335	0.883	0.008	0.000	0.017
55.....	1978.596	1978.827	1978.755	0.551	0.187	0.821	0.013	0.000	0.029
56.....	1978.827	1979.051	1978.980	0.865	0.514	1.166	0.014	0.002	0.026
57.....	1979.051	1979.150	1979.110	0.262	0.000	0.881	0.091	0.070	0.112
58.....	1979.150	1979.375	1979.304	0.879	0.331	1.451	0.137	0.101	0.172
59.....	1979.375	1979.586	1979.517	0.218	0.030	0.427	0.038	0.024	0.051
60.....	1979.586	1979.818	1979.746	0.000	0.000	0.197	0.038	0.024	0.052
61.....	1979.818	1980.065	1979.991	0.045	0.000	0.378	0.104	0.076	0.131
62.....	1980.065	1980.280	1980.211	0.000	0.000	0.262	0.080	0.055	0.104
63.....	1980.280	1980.450	1980.389	0.000	0.000	0.351	0.031	0.005	0.057
64.....	1980.450	1980.602	1980.546	0.508	0.186	0.747	0.009	0.000	0.020
65.....	1980.602	1980.737	1980.685	0.201	0.000	0.637	0.105	0.079	0.132
66.....	1980.737	1980.890	1980.834	0.333	0.000	0.374	0.000	0.000	0.199
67.....	1980.890	1981.059	1980.999	0.291	0.072	0.418	0.000	0.000	0.016
68.....	1981.059	1981.290	1981.218	0.349	0.127	0.503	0.003	0.000	0.010
69.....	1981.290	1981.519	1981.448	0.488	0.160	0.795	0.051	0.028	0.074
70.....	1981.519	1981.673	1981.616	0.038	0.000	0.301	0.051	0.032	0.071
71.....	1981.673	1981.826	1981.770	1.253	0.846	1.632	0.009	0.002	0.017
72.....	1981.826	1981.966	1981.913	0.643	0.314	0.941	0.007	0.000	0.015
73.....	1981.966	1982.210	1982.136	0.054	0.000	0.284	0.027	0.016	0.038
74.....	1982.210	1982.363	1982.307	0.424	0.187	0.653	0.010	0.002	0.017
75.....	1982.363	1982.810	1982.719	0.496	0.268	0.649	0.000	0.000	0.036
76.....	1982.810	1983.040	1982.969	0.411	0.146	0.551	0.000	0.000	0.029
77.....	1983.040	1983.194	1983.137	0.401	0.159	0.637	0.010	0.001	0.018
78.....	1983.194	1983.366	1983.305	0.661	0.331	0.872	0.004	0.000	0.013
79.....	1983.366	1983.531	1983.471	0.567	0.212	0.722	0.001	0.000	0.009
80.....	1983.531	1983.654	1983.605	0.836	0.480	1.120	0.000	0.000	0.043
81.....	1983.654	1983.884	1983.812	0.265	0.008	0.309	0.000	0.000	0.013
82.....	1983.884	1984.094	1984.026	0.434	0.163	0.689	0.026	0.008	0.044
83.....	1984.094	1984.250	1984.193	0.227	0.051	0.396	0.005	0.000	0.010
84.....	1984.250	1984.359	1984.315	0.545	0.237	0.815	0.004	0.000	0.010
85.....	1984.359	1984.551	1984.486	0.586	0.240	0.750	0.000	0.000	0.008
86.....	1984.551	1984.669	1984.622	1.199	0.821	1.548	0.000	0.000	0.041
87.....	1984.669	1984.920	1984.845	0.000	0.000	0.141	0.024	0.013	0.035
88.....	1984.920	1985.128	1985.060	0.215	0.048	0.393	0.013	0.006	0.021
89.....	1985.128	1985.337	1985.268	0.693	0.394	0.961	0.006	0.000	0.012
90.....	1986.772	1986.933	1986.875	0.939	0.499	1.225	0.011	0.000	0.027
91.....	1986.933	1987.123	1987.058	0.645	0.312	0.914	0.017	0.001	0.032
92.....	1987.170	1987.372	1987.305	0.967	0.572	1.337	0.031	0.015	0.047

TABLE 3—Continued

RUN	EXPOSURE TIMES			$^{37}\text{Ar}$ PRODUCED PER DAY			COUNTER BACKGROUND PER DAY		
	Start	Stop	Mean	Best Fit	68% Confidence Range		Best Fit	68% Confidence Range	
95 .....	1987.372	1987.541	1987.481	0.629	0.335	0.920	0.014	0.006	0.023
96 .....	1987.541	1987.796	1987.721	0.223	0.036	0.341	0.003	0.000	0.009
97 .....	1987.796	1987.944	1987.889	0.723	0.427	1.012	0.008	0.002	0.014
98 .....	1987.944	1988.155	1988.086	0.771	0.440	1.101	0.031	0.019	0.043
99 .....	1988.155	1988.289	1988.237	0.871	0.285	1.056	0.000	0.000	0.128
100 .....	1988.289	1988.480	1988.415	0.903	0.565	1.257	0.032	0.020	0.044
101 .....	1988.480	1988.669	1988.604	0.000	0.000	0.173	0.015	0.006	0.024
102 .....	1988.669	1988.808	1988.755	0.637	0.263	1.020	0.030	0.015	0.046
103 .....	1988.808	1988.963	1988.906	0.299	0.071	0.524	0.019	0.009	0.030
104 .....	1988.963	1989.193	1989.121	0.036	0.000	0.418	0.130	0.105	0.155
105 .....	1989.193	1989.455	1989.378	0.515	0.203	0.695	0.005	0.000	0.014
106 .....	1989.455	1989.645	1989.580	0.989	0.603	1.217	0.000	0.000	0.012
107 .....	1989.646	1989.769	1989.721	0.441	0.167	0.740	0.005	0.000	0.011
108 .....	1989.769	1989.952	1989.889	0.148	0.000	0.220	0.000	0.000	0.006
109 .....	1989.952	1990.098	1990.043	1.174	0.765	1.525	0.007	0.000	0.014
110 .....	1990.098	1990.347	1990.272	0.351	0.149	0.566	0.013	0.005	0.020
111 .....	1990.347	1990.517	1990.457	0.469	0.155	0.785	0.027	0.015	0.039
112 .....	1990.517	1990.668	1990.612	0.790	0.477	1.095	0.008	0.001	0.014
113 .....	1990.668	1990.838	1990.777	0.211	0.046	0.394	0.011	0.004	0.018
114 .....	1990.838	1991.052	1990.982	0.665	0.314	0.822	0.001	0.000	0.009
115 .....	1991.052	1991.265	1991.196	0.660	0.380	0.854	0.000	0.000	0.006
116 .....	1991.265	1991.418	1991.362	0.613	0.326	0.897	0.010	0.003	0.016
118 .....	1991.434	1991.566	1991.515	0.604	0.309	0.867	0.003	0.000	0.008
119 .....	1991.566	1991.742	1991.680	0.975	0.636	1.271	0.004	0.000	0.009
120 .....	1991.742	1991.892	1991.836	0.680	0.410	0.965	0.009	0.003	0.015
121 .....	1991.892	1992.070	1992.008	0.125	0.000	0.262	0.008	0.001	0.014
122 .....	1992.070	1992.236	1992.177	0.675	0.391	0.903	0.000	0.000	0.013
124 .....	1992.248	1992.447	1992.381	0.420	0.199	0.652	0.012	0.004	0.019
125 .....	1992.447	1992.638	1992.573	0.503	0.266	0.713	0.000	0.000	0.030
126 .....	1992.638	1992.789	1992.733	0.221	0.032	0.410	0.008	0.002	0.013
127 .....	1992.789	1992.942	1992.885	0.000	0.000	0.107	0.007	0.000	0.016
128 .....	1992.942	1993.235	1993.155	0.491	0.248	0.677	0.005	0.000	0.013
129 .....	1993.235	1993.361	1993.312	0.800	0.457	1.132	0.011	0.002	0.020
130 .....	1993.361	1994.023	1993.931	0.731	0.457	1.015	0.004	0.001	0.007
131 .....	1993.531	1994.185	1994.127	0.763	0.429	1.118	0.009	0.003	0.014
132 .....	1994.188	1994.388	1994.321	0.505	0.184	0.650	0.000	0.000	0.009

NOTE.—Mean exposure time is the average time of production of the atoms in the tank at the time of extraction; it is given by the expression  $t_{\text{mean}} = t_{\text{start}} + (1/\lambda) \ln [1/2 + (1/2)e^{\lambda(t_{\text{stop}} - t_{\text{start}})}]$ .

$N + 1$  tuple to have produced the observed data set, where the  $N + 1$  parameters are a single production rate  $p$  and individual background rates (in the proportional counter)  $b_i$  for each of the  $N$  runs. In the combined analysis, we have introduced the new assumption for the background half-life,  $\tau_b = 2.7$  yr.

#### 7.4. Statistical Uncertainties

The scale of the statistical uncertainty in an individual run can be estimated by using the usual Gaussian method. The number of neutrino-produced atoms in the tank at saturation is 25; a 60 day exposure results in 70% of saturation, or about 18 atoms present in the tank. An extraction efficiency of 95% and a gas processing efficiency of 96% means that 16 atoms are finally inserted into the counter. As the counting efficiency of a typical counter is about 0.42 for one FWHM, this results in about six observed  $^{37}\text{Ar}$  decays in the first three half-lives (105 days).

In order to get an idea of the background rate in the counter, we can look at the apparent signal rate after five half-lives. This is typically about one per 50 days. Thus, in the three half-life interval (105 days) considered above, we expect about two background events or a total of eight events that satisfy the  $^{37}\text{Ar}$  selection criteria. This gives a statistical uncertainty of  $(8 \pm 8^{1/2}) - (2 \pm 2^{1/2}) = 6 \pm 3$ , or approximately 50%.

$$\pm (10)^{1/2} = 6 \pm 3, \text{ or approximately } 50\%.$$

For the 108 runs, the global likelihood fit gives a total of 2200  $^{37}\text{Ar}$  atoms in the detector at the time of extraction. A total of 1997 atoms were eventually inserted into our proportional counters. These resulted in a total of 875 detected  $^{37}\text{Ar}$  decays within the two FWHM window, of which 766 are attributed to production by solar  $\nu_e$  and 109 to nonsolar processes. For a one FWHM selection window we have a total of 652 detected  $^{37}\text{Ar}$  decays, of which 571 are attributed to production by solar  $\nu_e$  and 109 to nonsolar processes.

The actual uncertainty quoted is determined from the likelihood function  $\mathcal{L}$ . Slightly different methods are used for determining the uncertainty in individual runs as opposed to that used for the combined results of multiple runs. For individual runs, the likelihood function  $\mathcal{L}$  is a function of only two parameters, the production rate,  $p$ , of neutrino-produced  $^{37}\text{Ar}$  in the tank and the rate of false  $^{37}\text{Ar}$  decay signals in the counter,  $b$ . The uncertainty in  $p$  is determined by integrating the probability distribution along the  $b$ -axis, which produces a one-dimensional probability distribution for the production rate  $p$  independent of the background in the counter. This probability distribution is frequently non-Gaussian in shape. The  $1\sigma$  uncertainty is found by determining the smallest range of the

parameter  $p$  (around the most likely value  $p_0$ ) that has a 68% chance of including the actual value of  $p$ . For runs where  $p_0$  is close to zero, this results in highly asymmetrical error bars.

For a set of combined runs, the likelihood function  $\mathcal{L}$  is the product of the likelihood functions of the individual runs. Because of the large number of events involved in the combined fit, the shape of the combined likelihood function near its maximum is very similar to that of a Gaussian (unlike the case of a single run). The uncertainty in this case is found by determining the shape of the likelihood function at this point and using this to determine the width of the appropriate Gaussian distribution for the parameter  $p$  (see Cleveland 1983 for additional details).

It should be noted that since some of the runs that are input into the multiple-run fit have distinctly non-Gaussian error distributions, it is not possible to take the results of the single run analyses and combine them to reproduce our multiple-run results, without using the underlying time series of selected events for each run.

### 7.5. Systematic Uncertainties

The systematic uncertainties that contribute to the chlorine measurement have been discussed in previous sections. Table 4 presents a summary of these contributions as they apply to a single observation and to the 108 run average.

For a single run, the systematic uncertainty, about 7%, is negligible compared to the 30%–50% statistical uncertainty. The systematic uncertainty becomes comparable to the statistical uncertainty when we determine the average solar neutrino flux by combining a large number of runs. In addition, combining runs reduces some of the systematic causes of uncertainty.

The uncertainty in the extraction efficiency for each observation is approximately 2.5%. (The contributions to the uncertainty in this parameter from its various components are discussed in detail in § 4.3.2.) Some of this uncertainty is correlated for several runs, such as volume calibrations and the isotopic composition of the carrier reservoirs, and some is not, such as pressure and temperature readings. Taking into account the relative portions that are correlated and uncorrelated and the fact that multiple measurements have been made of all of the uncorrelated components, we estimate that the systematic uncertainty in the extraction efficiency for the combination of 108 runs is 1.3%.

As discussed in Appendix B, the uncertainty in the counting efficiency for most observations is approximately 2.5%. Since many counters were used for several runs over a

long time span, they have a correlated contribution to the overall systematic uncertainty. To determine the contribution of an individual counter to this uncertainty, we allowed the efficiency of that counter to vary by its own uncertainty and then recalculated the cumulative  $^{37}\text{Ar}$  production rate. The deviation that resulted in the overall answer was then the contribution of that counter to the systematic uncertainty. This process was repeated for all counters and these deviations were then added in quadrature to give a total systematic uncertainty of 1.4%. This analysis neglected the fact that several counters were often calibrated using the same standardized source of  $^{37}\text{Ar}$  or used different sources of  $^{37}\text{Ar}$  standardized in the same large counter. These correlations, however, did not extend uniformly across the set of counters used in the Homestake experiment, as the counters were calibrated over a long time span using several standardization counters. As a worst-case scenario, we will assume a 0.5% correlated systematic error due to these causes and add this to the effects of the individual efficiency errors (which, combined in quadrature, gave an uncertainty of 1.4% in the final result), to give a total of 1.5% as the systematic error from the counting efficiency.

The major uncertainty in the overall production rate arises from the nonsolar neutrino background. As discussed in § 6, the value of this background varied with the experimental configuration. We determined its influence on the total systematic error in much the same way as was done for the counting efficiency, i.e., by allowing the nonsolar production rate for a particular configuration to vary by its own uncertainty, recalculating the overall production rate, and then adding these uncertainties in quadrature. The net result of that procedure is an uncertainty in the final result of +3.8%, –5.2%. This error is asymmetric due to the upper limit on  $\alpha$ -particle-induced production.

The final contribution to the systematic uncertainty arises from the assumed half-life of the decaying background component in the maximum likelihood fit to the counting data. We have used 2.7 yr, the half-life of  $^{55}\text{Fe}$ , in our analysis (see § 7.3). Fits to the slow data and the late data (where there should be no contribution from  $^{37}\text{Ar}$ ) indicate an uncertainty in this value of 0.7 yr ( $\sim 25\%$ ). Variation in the background half-life of this magnitude results in a variation in the resulting production rate calculated of 2%.

Including the 1.5% uncertainty due to event selection and combining these five uncertainty components in quadrature, we obtain a total systematic uncertainty for the combined production rate of (+5.0%, –6.1%). For simplicity, in the following we use the larger of the two extremes for both the positive and negative limits.

TABLE 4  
CONTRIBUTIONS TO SYSTEMATIC UNCERTAINTY

SOURCE	UNCERTAINTY	
	Per Run	For 108 Run Average
Extraction efficiency .....	Typically 2.5% (measured by run)	1.3%
Counting efficiency .....	2.5% (directly calibrated) 5% (indirectly calibrated)	1.5%
Nonsolar production rate.....	$^{+0.013}_{-0.021}$ atoms day $^{-1}$ (water shielded) $^{+0.028}_{-0.033}$ atoms day $^{-1}$ (no water shield)	$^{+0.018}_{-0.025}$ atoms day $^{-1}$
Event selection .....	5%–10% (dependent on selection cuts)	1.5%
Counter background time constant.....		2.0%

## 7.6. Measured Solar Neutrino Flux

The solar neutrino-induced  $^{37}\text{Ar}$  production rate in the Homestake chlorine detector is  $0.478 \pm 0.030$  (statistical)  $\pm 0.029$  (systematic) day $^{-1}$ . Since the detector contains  $2.16 \times 10^{30} \text{ }^{37}\text{Cl}$  atoms, this gives a neutrino capture rate of  $2.56 \pm 0.16$  (statistical)  $\pm 0.16$  (systematic)  $\times 10^{-36}$  per target atom s $^{-1}$  or  $2.56 \pm 0.16$  (statistical)  $\pm 0.16$  (systematic) SNU. This measurement is to be compared with the solar model predictions for the chlorine detector of  $9.3 \pm 1.3$  SNU (Bahcall & Pinsonneault 1995), 6.36 SNU (Turck-Chieze & Lopes 1993), and 7.64 SNU (Sackman, Boothroyd, & Fowler 1990). Clearly, the observed flux is much lower than that predicted. This discrepancy between observation and prediction has existed since the early 1970s when the observations of the Homestake detector were first reported.

Early comparisons of the Homestake chlorine detector observations and the predicted solar neutrino fluxes focused on the  ${}^8\text{B}$  neutrinos with the suggestion that this flux might be appreciably reduced. Once the data from the Kamiokande water Čerenkov detector became available, it appeared that the observed reduction in the  ${}^8\text{B}$  flux was probably only a factor of 2 and that the larger suppression of the chlorine signal indicated that a far more severe suppression existed for the electron neutrinos in the 1 MeV range, those from  ${}^7\text{Be}$ , *pep*, and the CNO cycle.

A considerable number of analyses of the combined observations of the four operating solar neutrino detectors, Homestake, Kamiokande, GALLEX, and SAGE, have been reported; see, for example Bludman et al. (1993); Fogli, Lisi, & Montanino (1994); Akhmedov, Lanza, & Petcov (1995); Berezinski, Fiorentini, & Lissia (1996); and Krastev & Petcov (1995). These analyses compare the observed signals with those predicted by solar models and generally conclude that the observed electron neutrino flux from  $^8\text{B}$  is about one-half of that predicted by the models, the electron neutrino flux from  $^7\text{Be}$  is less than 1/10 of that predicted, and the electron neutrino flux from  $p$ - $p$  reactions is consistent with that predicted.

The present chlorine detector measurement also permits us to establish an upper limit on the electron neutrino flux from  ${}^8\text{B}$  decays in the Sun of  $(2.25 \pm 0.21) \times 10^6 \nu_e \text{ cm}^{-2} \text{ s}^{-1}$ . To obtain this limit we assign the entire solar neutrino signal in our detector to  ${}^8\text{B}$ , divide the SNU measurement by the cross section for converting  ${}^{37}\text{Cl}$  into  ${}^{37}\text{Ar}$ ,

$(1.14 \pm 0.037) \times 10^{-42} \text{ cm}^2$ , and combine the statistical and systematic errors in quadrature.

A  ${}^8\text{B}$  neutrino flux measurement in a water Čerenkov detector, which observes the elastic scattering from electrons of all flavors of neutrinos, that is significantly larger than our upper limit for the electron neutrino flux from  ${}^8\text{B}$  would decisively demonstrate that non-electron flavor neutrinos from the Sun are reaching the Earth. This would be the first purely experimental demonstration that neutrino-flavor transformations are occurring. By subtracting our upper  ${}^8\text{B}$  electron neutrino flux limit from the most recent result of the SuperKamiokande measurement,  $(2.44 \pm 0.18) \times 10^6 \text{ v cm}^{-2} \text{ s}^{-1}$  (Totsuka 1997), we get a lower limit of  $[(0.19 \pm 0.19) \times 10^6] \times 6 \text{ v cm}^{-2} \text{ s}^{-1}$  for the nonelectron neutrino flux from  ${}^8\text{B}$  decays in the Sun, where the factor of 6 is because the electron-scattering cross section for nonelectron neutrinos is  $\frac{1}{6}$  of the cross section for electron neutrinos. Clearly, more precise flux measurements are required as the input for this quantity.

In the next year or two, the Sudbury Neutrino Observatory (SNO) should provide a direct measurement of the electron neutrino flux from  ${}^8\text{B}$ . Subtracting that flux from our result will, for the first time, provide an experimentally determined electron neutrino flux in the 1 MeV range. The anticipated precision of this experimentally determined electron neutrino flux in the 1 MeV region,  $\pm 0.19$  SNU, or  $0.4 \times 10^9 \nu_e \text{cm}^{-2} \text{s}^{-1}$ , should be sufficient to permit a sensitive determination of the magnitude of the solar electron neutrino flux suppression in this energy range and thus permit determination of the physical processes that are responsible for this suppression.

Finally, when these  $^7\text{Be}$ , *pep*, and CNO electron neutrino fluxes are combined with the gallium detector observations, we will at last obtain a solar neutrino emission spectrum that is completely experimentally determined, a goal that has long eluded us.

The authors would like to thank the National Science Foundation (grant AST 93-15293), the University of Pennsylvania Research Foundation, and the City University Research Foundation for their support of this work. We are deeply indebted to the Homestake Mining Company, both management and employees, for their continual assistance in the operation of this experiment and to J. C. Evans and J. K. Rowley for their participation.

## APPENDIX A

## MEASUREMENT OF EXTRACTION EFFICIENCY

This appendix explains how the extraction efficiency for each solar neutrino measurement is determined. The general principle is to insert a known volume (about  $0.1 \text{ cm}^3$  STP) of isotopically enriched argon gas into the  $\text{C}_2\text{Cl}_4$ -containing vessel at the beginning of the exposure period, and then to measure the volume and isotopic fractions of the argon gas that is removed from the proportional counter after counting is completed. The extraction efficiency is then set by comparing the volume of the argon isotope extracted and counted to the volume of the dominant carrier isotope that was inserted.

Since each extraction usually removes about 95% of the argon from the  $C_2Cl_4$ , the volume of argon that is collected in extraction  $n$  (called  $V_n$ ) can be considered as arising from the carrier added for that extraction (whose volume is  $C_n$ ) and from the carrier added for the preceding extraction (whose volume is  $C_{n-1}$ ). Defining  $e_n$  and  $e_{n-1}$  as the efficiency of removal of argon from the tank in extractions  $n$  and  $n - 1$ , respectively, and  $P_n$  as the processing efficiency in extraction  $n$ , i.e., the efficiency with which the argon sample, after removal from the tank, is transferred to the proportional counter, mass balance then gives the relationship

$$V_n = P_n e_n [C_n + (1 - e_{n-1}) C_{n-1}] + A_n ,$$

where  $A_n$  is the total volume of air argon in extraction  $n$ .  $A_n$  consists of the argon intentionally added to the counter filling to boost the counter pressure and any additional argon that has entered the sample by inleakage from the atmosphere. This basic equation applies for each of the three naturally occurring argon isotopes,  $^{36}\text{Ar}$ ,  $^{38}\text{Ar}$ , and  $^{40}\text{Ar}$ , whose fractions in air are 0.00337, 0.00063, and 0.99600, respectively. For a single extraction, this equation for the expected volume of extracted argon,  $V_n$ , thus yields three separate equations, one for each Ar isotope.

Since argon solubility equilibrium is attained in a time much shorter than the total extraction time, the efficiency of extraction from the tank,  $e_n$ , is related to the volume of helium,  $h_n$ , that flowed through the charcoal trap during extraction  $n$  by  $e_n = 1 - e^{-h_n/H}$ , where  $H$  is the gas extraction coefficient discussed in § 4.3.3. This relationship simplifies the three extraction equations so that they contain only the three variables,  $P_n$ ,  $H$ , and  $A_n$ . These equations are solved by equating the measured volume of each isotope of argon that was removed from the proportional counter at the end of counting and mass analyzed, which will be called  $M_n$ , to be equal to  $V_n$ . The air volume  $A_n$  is mainly determined by the  $^{40}\text{Ar}$  content of the measured sample, the processing efficiency  $P_n$  is mainly determined by the recovery of the carrier  $C_n$  added for extraction  $n$ , and the gas extraction coefficient  $H$  is determined by the recovery of the volumes of carrier  $C_{n-1}$  and  $C_n$ .

Figure 4 shows the gas extraction coefficient  $H$  determined in this manner for all extractions for which the isotopic analysis is available. The figure begins with extraction 29, the first extraction to use  $^{38}\text{Ar}$  as carrier. It is evident that the gas extraction coefficient has remained constant throughout the experiment. The average value is  $H = (1.31 \pm 0.03) \times 10^5$  liters, where the error is the standard deviation of the mean of the separate measurements. The fluctuations about the mean value are consistent with the known uncertainties of measurement, viz., a relative uncertainty of 1% in the volume of extracted argon and an absolute uncertainty of 0.5% in each of the isotopic fractions. This average value of  $H$  for the two decades of data taking agrees very well with the value of  $(1.31 \pm 0.02) \times 10^5$  liters determined from the initial purge of the tank (see § 4.4).

Since the gas extraction coefficient  $H$  is constant, it can be fixed at  $1.31 \times 10^5$  liters and the variables  $e_n$ ,  $e_{n-1}$ , and  $e_{n-2}$  can be eliminated from the extraction efficiency equation. For each extraction this yields three equations to be solved for the processing efficiency  $P_n$  and air volume  $A_n$ . These two variables are determined individually for extraction  $n$  by minimizing

$$\chi_n^2 = \sum_{i=1}^3 \left[ \frac{M_n(i) - V_n(i)}{\sigma_n(i)} \right]^2,$$

where the sum over  $i$  is for the three argon isotopes and the magnitude of the measurement errors  $\sigma_n(i)$  was stated in the preceding paragraph. The processing efficiency  $P_n$  determined for each extraction in this manner is shown in Figure 5. The error bars are derived from the error matrix in the standard manner (Press et al. 1992). The average value of  $\chi_n^2$  for all extractions is somewhat less than unity, indicating that the errors  $\sigma_n(i)$  are somewhat less than the assumed value of 0.5%.

The overall efficiency  $E_n$  with which the carrier gas is recovered in extraction  $n$  is the product  $P_n e_n = P_n (1 - e^{-h_n/H})$ . It is assumed that the fraction of neutrino-produced  $^{37}\text{Ar}$  that is extracted is identical to the fraction of carrier argon that is extracted, and thus  $E_n$  is used as the extraction efficiency in the analysis that determines the  $^{37}\text{Ar}$  production rate. The average value of  $E_n$  is 91.2% when the dominant carrier was  $^{36}\text{Ar}$  and 90.2% when the dominant carrier was  $^{38}\text{Ar}$ . The uncertainty in  $E_n$  is obtained by combining the errors in  $P_n$  and  $e_n$  in quadrature and has average values of 1.8% for  $^{36}\text{Ar}$  and 3.1% for  $^{38}\text{Ar}$  (the substantially larger error for  $^{38}\text{Ar}$  is believed to be because of its reduced natural abundance compared to  $^{36}\text{Ar}$ ). For those extractions for which isotopic analysis is not available, including the eight runs that were made before the procedure of alternating carrier from  $^{36}\text{Ar}$  to  $^{38}\text{Ar}$  was initiated, the average processing efficiency of 96.8% has been assumed.

The other parameter that is determined by this analysis is the volume of air in each extraction,  $A_n$ . If the volume of air argon that is intentionally added to the counter filling to raise the counter pressure is subtracted from  $A_n$ , the residual volume for a typical extraction is in the range of 0.1–0.2 cm<sup>3</sup> STP. In tests of the extraction system and the gas processing system, when they are isolated from the tank containing  $\text{C}_2\text{Cl}_4$ , very little atmospheric argon is recovered, implying that the recovered volume of air argon is associated in some way with the  $\text{C}_2\text{Cl}_4$ -containing vessel. Further, several extractions have been made with a short exposure time, from less than a day to a week. The volume of atmospheric argon obtained in such extractions is much less than the volume that is recovered during the normal exposure period of 2–3 months, indicating that there is a very small, but constant, leak of about 2  $\mu\text{l}$  of argon per day. This inleakage is mainly  $^{40}\text{Ar}$ , and contributes only 0.3  $\mu\text{l}$   $^{36}\text{Ar}$  and 0.06  $\mu\text{l}$   $^{38}\text{Ar}$  per run.

## APPENDIX B

### MEASUREMENT OF COUNTING EFFICIENCY

This appendix explains how the proportional counter efficiency for detecting  $^{37}\text{Ar}$  decays is measured. The general principle is to fill the counter with a gas sample that contains a calibrated number of  $^{37}\text{Ar}$  atoms and then to count the number of observed decays. Suitable quantities of  $^{37}\text{Ar}$  for counter calibration are easily made by irradiation of  $^{40}\text{Ca}$  by  $\geq 5$  MeV neutrons (Michael et al. 1984), such as those from a 1 Ci Pu(Be) or Ra(Be) neutron source. Several hours of exposure of a saturated solution of  $\text{CaCl}_2$  to a  $10^6$  neutron s<sup>-1</sup> source (the typical yield from 1 Ci of Pu) will produce  $\sim 5 \times 10^8$  atoms of  $^{37}\text{Ar}$ , giving  $10^2$  disintegrations s<sup>-1</sup>. The active argon is purified in a special vacuum system that is used only for handling moderately radioactive gas samples, diluted with inactive argon, and mixed with  $\text{CH}_4$ . This sample is used to calibrate several counters.

The absolute  $^{37}\text{Ar}$  activity is measured in large counters (internal volume of 100 cm<sup>3</sup> with an active region 30 cm long by 2 cm diameter) that are especially made for this purpose. The cathode is chemically deposited on the inside surface of the

counter envelope, thus eliminating any dead volume at the outside of the cathode. There are insulating guard rings around the anode wire outside the cathode region, resulting in a very well-defined active volume. The volume efficiency of these counters, defined as the ratio of the internal counter volume surrounded by the cathode to total internal volume, is directly measured by filling the counters with hexane to various levels and weighing them. The uncertainty in this measurement is determined by the precision with which the hexane level can be matched to the top and bottom of the cathode while filling (0.05 cm out of 30 cm, or about 0.2%) and by the precision of the mass measurement (0.1 g out of 60 g, or about 0.2% also). The total uncertainty in the volume efficiency of these counters is thus about 0.3%.

The absolute decay rate of a gas sample can be determined in such a counter by increasing the voltage on the cathode high enough that essentially all of the decays that take place inside the active volume are detected. At 1 atm, a high voltage of 2100 volts results in an energy threshold in the range of 30–50 eV, which is sufficient to detect all decays involving K- and L-Auger emission. Two small corrections to the total measured rate in such a counter are necessary to obtain the absolute decay rate. There is a 1.4% correction for  $^{37}\text{Ar}$  decays that deposit less than 50 eV (M-decays: 0.9% and K-decays with escape of the 2.816 keV X-ray: 0.5%), and there is a correction for the counter background (due to cosmic rays). The background is measured under identical counting conditions before the  $^{37}\text{Ar}$  sample is added and is approximately 1 count  $\text{s}^{-1}$ . The overall uncertainty in the absolute decay rate of a sample of  $^{37}\text{Ar}$  as determined by such measurements is then given by the combination of the volume efficiency (0.3%), the statistics of the decay measurement (0.3% for  $10^5$  decays observed), the background subtraction (0.005%), and the branching ratio correction (0.25%), for a total uncertainty of 0.5%.

The accuracy of the determination of the absolute decay rate by means of the large standardization counter may be tested by using  $^{127}\text{Xe}$ . This isotope has much in common with  $^{37}\text{Ar}$ : it is a rare gas that decays by electron capture, with an almost identical half-life. However, unlike  $^{37}\text{Ar}$ ,  $^{127}\text{Xe}$  is forbidden by spin considerations from decaying directly to the nuclear ground state of  $^{127}\text{I}$ . Thus the atomic signal produced in the proportional counter due to Auger or X-ray emission from the rearrangement of electrons is accompanied by the emission of gamma rays due to nuclear rearrangement. Observation of these coincident gamma rays in a NaI crystal that surrounds the proportional counter allows a direct determination of the absolute decay rate of a sample of  $^{127}\text{Xe}$ . Neither the proportional counter nor the NaI crystal will have 100% efficient detection; the singles rate in each detector will be given by

$$\begin{aligned} R_{\text{counter}} &= \epsilon_{\text{counter}} R_{\text{abs}}, \\ R_{\text{NaI}} &= \epsilon_{\text{NaI}} R_{\text{abs}}, \end{aligned}$$

where the  $\epsilon$ 's are the efficiency of each detector, and  $R_{\text{abs}}$  is the absolute decay rate. The rate of coincident events detected is given by

$$R_{\text{coin}} = \epsilon_{\text{counter}} \epsilon_{\text{NaI}} R_{\text{abs}}.$$

Comparing the product of the two singles rates to the coincident rate eliminates the unknown efficiencies of each detector and determines the absolute rate of decay:

$$\frac{R_{\text{counter}} R_{\text{NaI}}}{R_{\text{coin}}} = \frac{\epsilon_{\text{counter}} \epsilon_{\text{NaI}} R_{\text{abs}}^2}{\epsilon_{\text{counter}} \epsilon_{\text{NaI}} R_{\text{abs}}} = R_{\text{abs}}.$$

The absolute decay rate of a sample of  $^{127}\text{Xe}$  has been determined with this method and compared to the rate determined for the same gas sample in one of the large standardization counters. The two rates agreed to within 0.25%, thus providing a check on the procedure for determining the proportional counter volume efficiency.

For each counter whose efficiency is to be measured, an energy spectrum using the calibrated  $^{37}\text{Ar}$  source is taken with the threshold at 500 eV or less and saturation at about 5 keV. (A sample spectrum appears in the main text.) The dominant spectral feature is a symmetric full-energy peak at 2.82 keV, together with an approximately constant tail produced by degraded events occurring in the fringe field regions of the counter. The background of the proportional counter during calibration is almost solely from cosmic rays and is insignificant, about 1 count per minute above 500 eV.

These counter spectra are analyzed by decomposing them into a Gaussian and a flat background produced by degraded events below the Gaussian peak. Specifically, they are fit with the function

$$f(E) = A \{ \exp(-T^2) + B[1 - \tan h(T)] \},$$

where  $T = (E - E_c)/2^{1/2}S$ , and  $S$  is the standard deviation of the Gaussian. The fit is made over an energy range of approximately 1.0–3.8 keV, which is chosen to totally include the K-peak but to exclude the L-decays at 0.3 keV. The three parameters of the Gaussian (amplitude  $A$ , center  $E_c$ , and width  $S$ ), and the amplitude of the degraded event term  $B$  are all varied to minimize chi-square. Good fits (chi-square per degree of freedom from 0.8 to 1.4) are usually obtained, and the constant  $B$  is typically 0.025. Using the center and width of the Gaussian as determined from the fit, the number of counts in the input spectrum inside a chosen spectral region is determined by summation. The counter efficiency is then the ratio of the measured count rate in this energy region to the absolute count rate of this gas sample, with appropriate correction for sample volume and decay between the different times of measurement. For some counters the counting efficiency has been measured at rates from 100 to 0.1  $\text{s}^{-1}$ , and no rate dependence of the efficiency has been observed. Measurements are usually made at approximately the same filling pressure as is used for counting of the Homestake samples, 950 mm Hg, but the efficiency changes very slightly with pressure, with only a 2% increase for a pressure increase from 760 to 1520 mm Hg.

Typical values of counting efficiency are 54% inside two FWHM and 42% inside one FWHM. The uncertainties in these efficiencies are a combination of the uncertainty in the absolute decay rate of the sample (0.5%, as discussed earlier), the statistics of the sample spectrum (about 0.7% for 20,000 events in a given spectral region), the determination of the spectral

parameters of the sample spectrum (about 0.5%), the uncertainty in measuring the volume of the sample inserted into the miniature proportional counter compared to that inserted into the large standardization counter (about 2%), and variations that arise due to pressure and volume differences in individual fillings of the counter (1%), giving a total relative uncertainty in the counter efficiency of 2.5%.

## REFERENCES

- Akhmedov, E. K., Lanza, A., & Petcov, S. T. 1995, Phys. Lett. B, 348, 124  
 Alvarez, L. W. 1949, University of California Radiation Laboratory Report, UCRL-328  
 Aufderheide, M. B., Bloom, S. D., Resler, D. A., & Goodman, C. D. 1994, Phys. Rev. C, 49, 678  
 Bahcall, J. N. 1964, Phys. Rev. Lett., 12, 300  
 ———. 1978, Rev. Mod. Phys., 50, 881  
 ———. 1989, Neutrino Astrophysics (Cambridge: Cambridge Univ. Press)  
 Bahcall, J. N., & Barnes, C. A. 1964, Phys. Lett., 12, 48  
 Bahcall, J. N., et al. 1996, Phys. Rev. C, 54, 411  
 Bahcall, J. N., Bahcall, N. A., & Shaviv, G. 1968, Phys. Rev. Lett., 20, 1209  
 Bahcall, J. N., & Davis, R., Jr. 1976, Science, 191, 264  
 ———. 1982, in Essays in Nuclear Astrophysics, ed. C. A. Barnes, D. D. Clayton, & D. Schramm (Cambridge: Cambridge Univ. Press), 243; reprinted in Bahcall, J. N. 1989, Neutrino Astrophysics (Cambridge: Cambridge Univ. Press), 487  
 Bahcall, J. N., & Pinsonneault, M. H. 1995, Rev. Mod. Phys., 67, 781  
 Barabanov, I. R., Gavrin, V. N., Zatsepin, G. T., Orekov, I. V., & Prokop'eva, L. P. 1983, Atomnaya Energiya, 54, 136  
 Berezhinsky, V., Fiorentini, G., & Lissia, M. 1996, Phys. Lett. B, 365, 185  
 Beulow, S. J., Worsnop, D. R., & Herschbach, D. R. 1981, Proc. Nat. Acad. Sci., 78, 7250  
 Bludman, S. A., Hata, N., Kennedy, D. C., & Langacker, P. G. 1993, Phys. Rev. D, 47, 2220  
 Cameron, A. G. W. 1958, Ann. Rev. Nucl. Sci., 8, 299  
 Cassiday, G. L. 1973, Proc. 13th Int. Cosmic-Ray Conf. (Boulder), 3, 1958  
 Cleveland, B. T. 1983, Nucl. Inst. Methods, 214, 451  
 Cleveland, B. T., Daily, T. M., Davis, R., Jr., Distel, J., Lande, K., Lee, C. K., Wildenhain, P. S., & Ullman, J. 1995, Nucl. Phys. B (Proc. Suppl.), 38, 47  
 Cleveland, B. T., Davis, R. Jr., Fireman, E. L., & Rowley, J. K. 1998, in preparation  
 Cleveland, B. T., Davis, R., Jr., & Rowley, J. K. 1980, in AIP Conf. Proc. 72, Weak Interactions as Probes of Unification, ed. G. B. Collins, L. N. Chang, & J. R. Ficenc (New York: AIP), 322  
 Cleveland, B. T., et al. 1990, Proc. 25th Int. Conf. on High Energy Phys., ed. K. K. Phua & Y. Yamaguchi (Singapore: World Scientific), 1, 667  
 Clever, H. L., Battino, R., Saylor, J. H., & Gross, P. M. 1957, J. Chem. Phys., 61, 1078  
 Davis, R., Jr. 1978, in Proc. of the Informal Conf. on the Status and Future of Solar Neutrino Research (BNL Report 50879), ed. G. Griedlander (Upton NY: Brookhaven National Laboratory), 1  
 ———. 1993, Proc. 23rd Int. Cosmic-Ray Conf. (Calgary) 3, 869  
 ———. 1994a, Prog. in Nuc. and Part. Phys., 32, 13  
 ———. 1994b, in Proc. 6th Int. Workshop on Neutrino Telescopes, ed. M. Baldo Ceolin (Venice: Univ. of Padua)  
 Davis, R., Jr., Cleveland, B. T., & Rowley, J. K. 1982, in AIP Conf. Proc. 96, Science Underground, ed. M. M. Nieto, W. C. Haxton, C. M. Hoffman, E. W. Kolb, V. D. Sandberg, & J. W. Toews (New York: AIP), 2  
 Davis, R., Jr., Evans, J. C., Radeka, V., & Rogers, L. 1972, in Proc. 3rd Int. Conf. on Neutrino Physics and Astrophysics, ed. A. Frenkel & G. Marx (Budapest: OMKDT-Technoinform), 51  
 Davis, R., Jr., Harmer D. S., & Hoffman, K. C. 1968, Phys. Rev. Lett., 20, 1205  
 Domogatskii, G. V., & Eramzhyan, R. A. 1977, Iz. Akademii Nauk SSSR, Ser. Fizicheskaya, 41, 1969  
 Fink, R. W. 1972, Rev. Mod. Phys., 44, 716  
 Fireman, E. L., Cleveland, B. T., Davis, R., Jr., & Rowley, J. K. 1985, in AIP Conf. Proc. 126, Solar Neutrinos and Neutrino Astronomy, ed. M. L. Cherry, K. Lande, & W. A. Fowler (New York: AIP), 22  
 Fogli, G. L., Lisi, E., & Montanino, D. 1994, Phys. Rev. D, 48, 3626  
 Fowler, W. A. 1958, ApJ 127, 551  
 Gaisser, T. K., & Stanev, T. 1985, in AIP Conf. Proc. 126, Solar Neutrinos and Neutrino Astronomy, ed. M. L. Cherry, K. Lande, & W. A. Fowler (New York: AIP), 277  
 Garcia, A., et al. 1991, Phys. Rev. Lett., 67, 3654  
 Goodman, C. D., et al. 1980, Phys. Rev. Lett., 44, 1755  
 Gromov, F. V., Kopylov, A. V., Novikova, G. Y., & Orekhov, I. V. 1978, in Proc. Int. Conf. on Neutrino Physics and Neutrino Astrophysics, ed. M. A. Markov, G. V. Domogatsky, A. A. Komar, & A. N. Tavkhelidze (Moscow: Nauka), 1, 73  
 Holmgren, H. D., & Johnston, R. L. 1959, Phys. Rev., 113, 1556  
 Jacobs, K. C. 1975, Nature, 256, 560  
 Krastev, P. I., & Petcov, S. T. 1995, Nucl. Phys. B, 449, 605  
 Lande, K., et al. 1991, in AIP Conf. Proc. 243, Intersections between Particle and Nuclear Physics, ed. W. T. H. van Oers (New York: AIP), 1122  
 Leventhal, J. J., & Friedman, F. 1972, Phys. Rev. D, 6, 3338  
 Michael, H., Wolfe, R., & Qaim, S. M. 1984, Int. J. Appl. Radiat. Isot., 35, 813  
 Opendak, M., & Wildenhain, P. S. 1992, Nucl. Inst. Methods, 345, 570  
 Pontecorvo, B. 1946, Chalk River Report, PD-205  
 Press, W. H., Teukolsky, S. A., Vetterling, W. T., & Flannery, B. P. 1992, Numerical Recipes (Cambridge: Cambridge Univ. Press)  
 Rowley, J. K., Cleveland, B. T., & Davis, R., Jr. 1984, in AIP Conf. Proc. 126, Solar Neutrinos and Neutrino Astronomy, ed. M. L. Cherry, K. Lande, & W. A. Fowler (New York: AIP), 1  
 Rudzskii, M. A., & Seidov, Z. F. 1979, Yad. Fiz., 30, 1063  
 Ruiz, H. V., & Davis, R., Jr. 1978, Acta Cient. Venezolana, 29, 415  
 Ryazhskaya, O. G. 1991, Sov. Phys. JETP Lett., 53, 135  
 Ryazhskaya, O. G., & Zatsepin, G. T. 1965, Proc. 9th Int. Cosmic-Ray Conf. (London), 2, 987  
 Sackman, J., Boothroyd, A. I., & Fowler, W. A. 1990, ApJ 360, 727  
 Saylor, J. H., & Battino, R. 1958, J. Chem. Phys., 22, 1334  
 Spannagel, G., & Fireman, E. 1972, J. Geophys. Res., 77, 5351  
 Totsuka, Y. 1998, in Int. Symp. on Lepton and Photon Interactions at High Energies (Hamburg) (Amsterdam: North-Holland), in press  
 Trimble, V., & Reines, F. 1973, Rev. Mod. Phys., 45, 1  
 Turck-Chieze, S., & Lopes, I. 1993, ApJ, 408, 347  
 Wells, D. P. 1992, Bull. Am. Phys. Soc., 37, 1296  
 Wolfendale, A. W., Young, E. C. M., & Davis, R., Jr. 1972, Nature Phys. Sci., 238, 130  
 Zatsepin, G. T., Kopylov, A. V., & Shirokova, E. K. 1980, Iz. Akad. Nauk SSSR, Ser. Fizicheskaya, 44, 622